Eindhoven University of Technology

MASTER

Photovoltaic energy harvesting from metal flames

van Herwijnen, Stefan A.H.

Award date:
2018

Link to publication

Master's thesis

Photovoltaic energy harvesting from metal flames

S.A.H. van Herwijnen

Supervisors:

Prof. L.P.H. de Goey and dr. Y.L. Shoshin
Eindhoven University of Technology
Faculty of Mechanical Engineering
Section Multiphase and Reactive Flows

June 7, 2018

Abstract

In order to reduce our carbon footprint, metal fuels have recently been proposed as a clean and renewable energy carrier. At this point, harvesting the energy from metal fuels is one of the key issues. As metal flames have a high temperatures and thus a large radiative energy loss, the use of a photovoltaic system is proposed to harvest this energy. Magnesium is particularly interesting for this purpose because of its radiative properties. By measuring the power and spectrum of magnesium flames, it is shown that for small magnesium samples approximately 28% of heat is lost by radiation. The spectrum of a magnesium flame is estimated to have a spectral efficiency of 33% in combination with a silicon photovoltaic cell. With current solar cell technology, it is estimated that an overall efficiency of 5% should be achievable for a photovoltaic system for metal flames. This efficiency can likely be greatly increased by controlling the combustion process and choosing the appropriate photovoltaic cells.

Acknowledgements

There were quite some obstacles on my way to finish this thesis, and I would not have been able to do it on my own. In particular I would like to thank Yuriy Shoshin and Jasper Hoek for directing and helping me with the experiments. Furthermore, I am also grateful for the help of Theo de Groot and Martin Huijzer for their help with the lab equipment. And of course thanks to Philip de Goey and Marijke Creusen for their understanding and support.

Contents

List of Figures

List of Tables

List of Symbols

Symbols

Symbol	Quantity	Unit
A	Surface area	$\mathrm{m^2}$
B_λ	Spectral radiance	$\mathrm{W\,nm^{-1}\,m^{-2}\,sr^{-1}}$
C	Calibration file	$\mathrm{\mu J\,count^{-1}}$
D	Raw dark spectrum	counts
E	Energy	J
$I_{e,\lambda}$	Spectral irradiance	$\mathrm{W\,nm^{-1}\,m^{-2}}$
I_e	Irradiance	$\mathrm{W\,m^{-2}}$
I	Current	A
P	Power	W
S	Raw spectrum	counts
T	Temperature	K
V	Voltage	V
ΔH_f	Enthalpy of formation	$\mathrm{kJ\,mol^{-1}}$
Ω	Solid angle	sr
Φ_p	Photon flux	$\mathrm{s^{-1}}$
ϵ	Emissivity	-
η	Efficiency	-
λ	Wavelength of light	m
ν	Frequency of light	$\mathrm{s^{-1}}$
ϕ	Azimuthal angle	rad
σ	Stefan-Boltzmann constant, $\sigma = 5.67 \times 10^{-8}\,\mathrm{W\,m^{-2}\,K^{-4}}$	$\mathrm{W\,m^{-2}\,K^{-4}}$
θ	Polar angle	rad
b	Wien's displacement constant, $b = 2.898 \times 10^{-3}\,\mathrm{m\,K}$	m K
c	Velocity of light	$\mathrm{m\,s^{-1}}$
d	Thickness of the sensor	m
h	Planck constant, $h = 6.626\,070\,04 \times 10^{-34}\,\mathrm{m^2\,kg\,s^{-1}}$	$\mathrm{m^2\,kg\,s^{-1}}$
k_B	Boltzmann constant, $k_B = 1.380\,648 \times 10^{-23}\,\mathrm{J\,K^{-1}}$	$\mathrm{J\,K^{-1}}$
k	Isotropy factor	-
r	Radius	m
t	Time	s

Subscripts

after	After absorption or emission of a photon
aperture	Property of the aperture
before	Before absorption or emission of a photon
e	electronic
flame	Property of the flame
internal	Property contained within a molecule
max	maximum
meas	measured
mp	maximum power
oc	open-circuit

ph	Property of a photon
pixel	pixel
plate	Property of the absorber plate
probe	Property of the spectrometer probe
pv	Property of the photovoltaic system
r	rotational
rad	radiated
sc	short-circuit
tot	total
v	vibrational
vis	Property in the visible range

1 Introduction

The tackling of climate change is increasingly accepted as one of the main challenges in our current and future society. Slowly but steadily, the world is transitioning from fossil fuels to renewable energy sources. As stated by Bergthorson, Goroshin, Soo, *et al.*, a complete transition to a low-carbon society is currently prevented by the lack of clean and renewable energy carriers [1]. They propose metal as such an energy carrier. Amongst recycling and transportation, energy production from metal fuels is one of the key issues. Direct combustion of metal powder seems to be most promising approach [1]. However, this does require an effective method to harvest the energy from the flame.

One of the properties of metal combustion is a high flame temperature, and as a result, a large radiative energy loss. In the case of magnesium, Shoshin and Altman have shown that the radiated energy is approximately 40% of the total heat release [2]. By harvesting this radiated energy with photovoltaics, a simple energy production method from metal fuels is obtained.

In this report the efficiency of harvesting energy from metal flames by means of photovoltaics is examined. Magnesium is the metal of choice in this research due to its highly radiative flame. The goal of this report is to characterize the radiation of a magnesium flame and analyze the achievable efficiency in combination with a photovoltaic cell. Based on the results, the feasibility of this energy harvesting method will be assessed.

2 Metal powder combustion

Before getting into the details of harvesting energy from metal flames, it is important to understand why metal powder combustion is researched.

This chapter will provide the background information of metal fuels and metal combustion. For this research project, the focus will be on magnesium.

Firstly, it is explained why metals can be used as a clean and recyclable fuel. Secondly, the combustion modes of metal powder are examined, with magnesium in particular. Finally, multiple methods of harvesting energy from metal flames are examined.

2.1 Clean and recyclable fuels

Up to this day fossil fuels are the main source of energy. Fossil fuels exist in different forms, e.g. coal, oil and natural gas. These fuels differ to a great extent, but they have in common that they are carbon based. This means that carbon oxides are created upon combustion. Furthermore, these fuels are not sustainable and it is inevitable that the sources will be depleted in the future.

There are multiple ways to generate clean energy by harnessing wind, geothermal, solar or hydro power. However, what is lacking for any of those clean energy sources is a clean and recyclable energy carrier. Batteries and hydrogen are often proposed as future energy carriers, but batteries are a poor energy carrier and hydrogen is accompanied by large energy losses when used as a fuel [3]. Figure 2.1 shows the volumetric and gravimetric energy densities of various fuels.
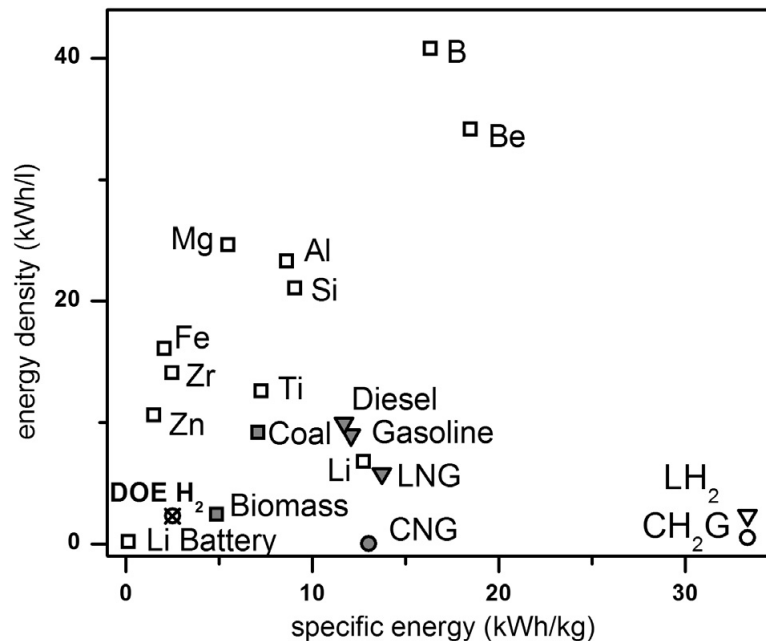
Figure 2.1: Volumetric and gravimetric energy density for various metal fuels compared to batteries, hydrogen, bio-derived fuels, and fossil fuels. Hydrogen has a large specific energy but, a poor energy density. Compared to fossil fuels, a lithium battery is also a poor energy carrier. Most metals have a larger energy density than fossil fuels, but a slightly worse specific energy.
Reprinted from Bergthorson, Goroshin, Soo, *et al.*, "Direct combustion of recyclable metal fuels for zero-carbon heat and power" [1].

As shown in the figure, lithium batteries are a poor choice for an energy dense energy carrier. Hydrogen (liquefied or compressed) on the other hand has a large specific energy, but a low energy density and more importantly, it is extremely flammable and hard to store.

Regardless of the alternative fuel that will be used, in order to make it a success, a different view on fuels is required. Traditional fuels are used as an energy source, i.e. the energy is subtracted and the waste is disposed. It should be clear that this is a non-sustainable approach. The new view on fuels should be that of an energy carrier instead of an energy source. That means that the fuels will store energy in a cyclic manner. Perhaps the easiest method of grasping this idea is to think of a battery. Future fuels will fulfill the same task, but in a different way.

2.1.1 Metal as energy carrier

As shown in Figure 2.1, metals have a large energy density. Boron provides the most favorable energy density and specific energy, however it is rare and expensive which means it is unsuitable as a replacement for fossil fuels. Better candidates are abundant metals such as silicon, aluminium, iron and magnesium.

Metals can be used to produce hydrogen. When exposed to water, the metals will react according to Equation (2.1).

$$x\,M + y\,H_2O \longrightarrow M_xO_y + y\,H_2 \tag{2.1}$$
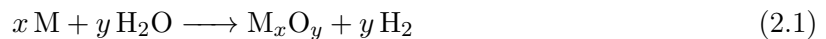
In this equation M stands for an arbitrary metal. By generating hydrogen using this method, the benefits of hydrogen fuel can be harnessed without the disadvantages of storing compressed or liquefied hydrogen. However, the metal-water reaction is relatively slow at moderate temperatures and pressures. This means that it is unusable for high-power applications [1].

A different method of releasing the contained energy in metal fuels is by direct combustion. The metal will react with oxygen and form a metal-oxide, of which an example is shown in Equation (2.2).

$$2\,M + O_2 \longrightarrow 2\,MO \tag{2.2}$$

Again, M stands for an arbitrary metal in this equation. Bergthorson, Goroshin, Soo, *et al.* have explained the physical properties of direct combustion of metal in air. A short summary is provided in the next section.

2.2 Combustion modes

Bergthorson, Goroshin, Soo, *et al.* group the combustion of small metal particles in the small Biot number regime into three modes (A, B and C):

- Mode A is described as a metal droplet surrounded by a micro-flame. Metal vapor and the oxidator are transported to the flame front where the combustion takes place. The formed oxides condense at the outer side of the flame front.

- In mode B gaseous metal oxides or sub-oxides will form at the droplet surface and diffuse away from the droplet. At some distance from the droplet, the formed oxides and sub-oxides will condense or react.

- In contrast to mode B, the oxide products will be formed directly on the droplet surface in mode C. The resulting particle size will be larger than the initial particle size.

The three modes are visualized in Figure 2.2.
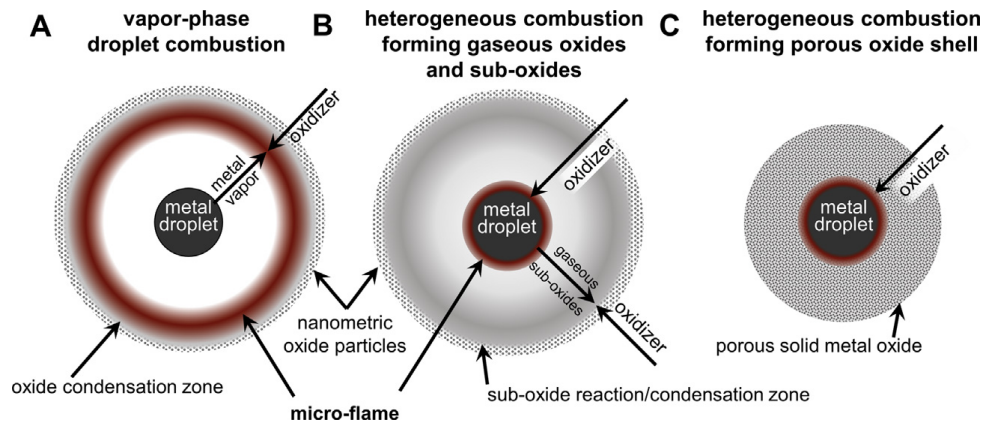
Figure 2.2: Modes of particle combustion in the small Biot number regime.
Reprinted from Bergthorson, Goroshin, Soo, *et al.*, "Direct combustion of recyclable metal fuels for zero-carbon heat and power" [1].

Mode A occurs for metals which have a flame temperature higher than their boiling point. Modes B and C occur for metals with a flame temperature lower than their boiling point. Figure 2.3 shows a classification of the combustion modes based on thermodynamic calculations.
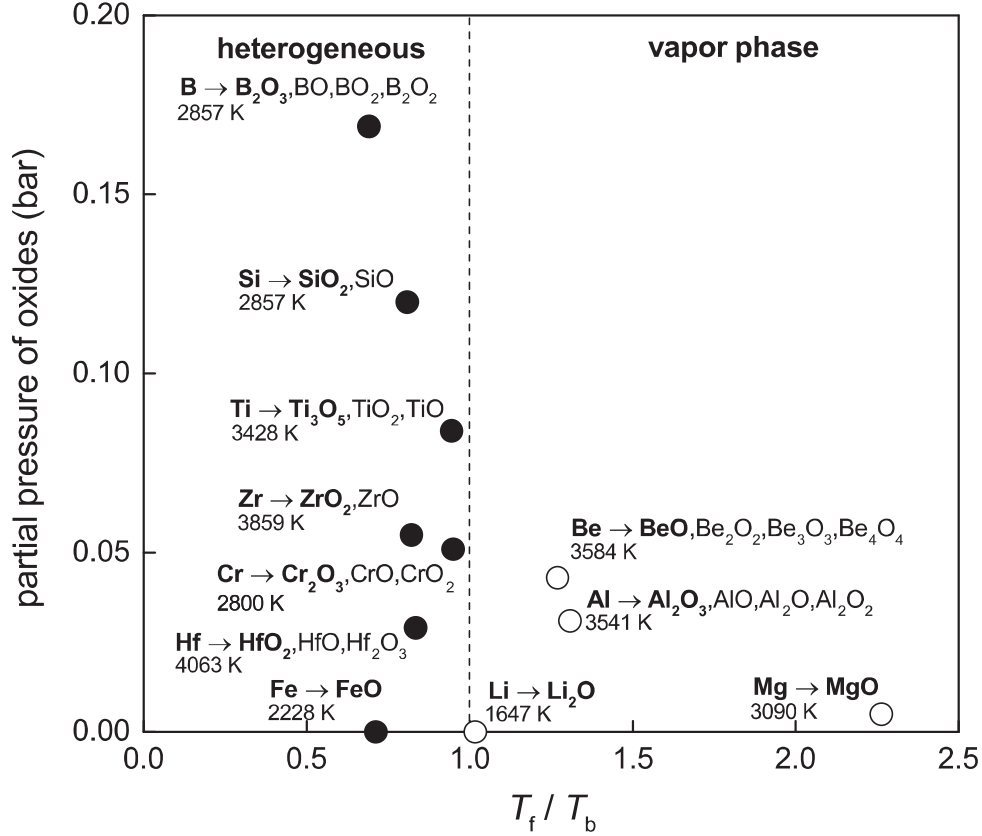
Figure 2.3: Classification of metal particle combustion modes based on the ratio of the flame temperature and boiling point and the partial pressure of the metal oxides. Metals with a flame temperature higher than their boiling point will burn in mode A. Reprinted from Bergthorson, Goroshin, Soo, *et al.*, "Direct combustion of recyclable metal fuels for zero-carbon heat and power" [1].

The figure shows that aluminium and magnesium are expected to burn in mode A. Metals with a flame temperature lower than their boiling point will burn in mode C only when the partial pressure of oxides is below 10^{-4} bar. This means that iron is the only metal that burns in mode C. However, classifying the metals into combustion modes by its physical and chemical properties is a simplification of the actual process. Research has shown that the combustion mode can be controlled by varying the combustion parameters [1]. The following section will provide more detailed information about the combustion process of magnesium.

2.2.1 Magnesium

Under the proper circumstances, magnesium reacts with oxygen to form magnesium oxide:

$$2\,\mathrm{Mg} + \mathrm{O_2} \longrightarrow 2\,\mathrm{MgO}$$
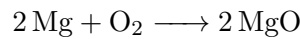
This reaction will be the primary reaction for direct combustion of magnesium. However, it is only one of the many reactions that (may) occur during the combustion of magnesium [4]. As a result of the high flame temperature, there will potentially be a significant NOx production. Magnesium itself will also react with nitrogen according to the following reaction:

$$3\,\mathrm{Mg} + \mathrm{N_2} \longrightarrow \mathrm{Mg_3N_2}$$
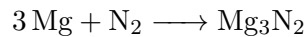
Magnesium will also strongly react with water to produce hydrogen:

$$\mathrm{Mg + 2\,H_2O \longrightarrow Mg(OH)_2 + H_2}$$
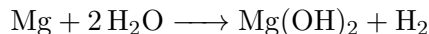
Due to the higher reaction speed, trying to extinguish a magnesium fire with water will result in rapid production and combustion of hydrogen. In addition, magnesium will also react with carbon dioxide:

$$\mathrm{2\,Mg + CO_2 \longrightarrow 2\,MgO + C}$$
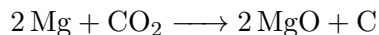
The properties of magnesium mentioned above is the reason that most research on magnesium flames is focused on extinguishing them. Even silicon dioxide (a major constituent of sand) will react with magnesium:

$$\mathrm{2\,Mg + SiO_2 \longrightarrow 2\,MgO + Si}$$
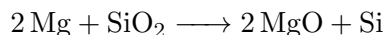
Both the advantage as well as the disadvantage of these properties is that magnesium does not require oxygen gas to burn. This enables the combustion of magnesium in environments without air or oxygen, but also makes it difficult to extinguish a magnesium fire. The fire can only be extinguished by cutting either the fuel or oxygen supply directly. Both these options are difficult or impossible to achieve in conventional (combustion) environments.

As explained in Section 2.2, magnesium is expected to burn in mode A. However, in reality the combustion mechanism is more complicated. Dreizin, Berman, and Vicenzi have researched the combustion behavior of magnesium in air [5][6]. They observed that hydrogen is contained within the magnesium that is released upon the melting of the magnesium. This hydrogen is thought to effect the particle shape and to play a role in the ignition of magnesium. From their research they concluded that magnesium will burn by two mechanisms. The first is a vapor-phase reaction around a molten magnesium particle. This reaction is insufficiently fast to deplete all oxygen, and as a result oxygen will diffuse into the molten magnesium droplet to form a new phase: liquid $\mathrm{Mg - O_{solution}}$. This reaction starts simultaneously with the vapor-phase combustion, but will become the primary reaction mechanism once the vapor-phase flame stops. When the solution becomes saturated, an exothermic phase separation will occur.

The above implies that an oxide in the vapor phase as well as in the solid phase is produced. Cassel and Liebman observed that initially magnesium oxide in the vapor phase is produced, which eventually leads to supersaturation [7]. This will result in nucleation and precipitation which forms solid magnesium oxides. This explains the origin of the white smoke as well as ash produced by magnesium combustion. However, they also concluded that more research is required to fully understand the combustion mechanism.

Another interesting property of magnesium is that it is easy to ignite. The flame temperature of magnesium is similar to that of aluminium, but an aluminium particle has an ignition temperature of approximately $2000\,\mathrm{K}$ ([8]) whereas the ignition temperature of a magnesium particles is only around $1000\,\mathrm{K}$ ([9]). This is the reason why magnesium is often used as a fire starter. It will produce a high temperature flame which can be ignited by a low temperature.

Garra, Leyssens, Allgaier, *et al.* have researched the feasibility of magnesium powder as an energy carrier at pilot scale [10]. They have analyzed short time stable magnesium/air flames in a combustion chamber using magnesium powder of $20\,\mathrm{\mu m}$ to $50\,\mathrm{\mu m}$ and $50\,\mathrm{\mu m}$ to $70\,\mathrm{\mu m}$. First of all, they concluded that the NOx emissions are higher for the smaller particle sizes. They

have attributed this to the fact that for larger particles the heat release during the combustion process will be slower. This will result in a lower temperature and thus lower thermal NOx emissions. The measured NOx emissions were up to ten times higher than that of a conventional diesel engine. However, they emphasize that their combustion chamber was not optimized for low NOx emissions and that after-treatment systems can effectively be used for magnesium/air combustion. Secondly, they concluded that the majority of particles produced after the combustion process were larger than 1 µm and could effectively be captured by a cyclone. It seems that even though magnesium is expected to burn in mode A (vapor phase droplet combustion), it may actually burn in mode C (porous oxide shell formed on the droplet surface) under the right circumstances.

Finally, the most interesting property of magnesium for this research project is the fact that a magnesium flame is highly radiative. It has been shown that energy radiated from a burning magnesium particle is nearly a constant fraction of 40% of the total energy release [2]. The large radiative heat transfer is determined by the ultrafine magnesia that is produced upon the combustion of magnesium [11]. Shoshin and Altman concluded that the magnesium particle flame emissivity is controlled by the natural gas convection. They have shown that the emissivity is inversely proportional to the mean gas convection velocity in the flame region. In turn, the convection velocity is proportional to the initial particle radius which means that smaller particles will have a larger emissivity.

2.3 Energy harvesting from metal flames

One of the key problems into making metal powder a successful renewable energy carrier is finding an efficient way to harvest the energy released upon combustion. The obvious choice would be to use a heat engine. However, compared to combustion of hydrocarbon fuels in air, there are two major differences:

1. In contrast to hydrocarbon fuels, both the metal as its combustion products are solids. While this allows for easier capture of the combustion products (in order to recycle them), it could cause a major problem by means of erosion. Metal fuels can easily be transported in a stream of air, but this requires a constant stream and the particles inside the stream could erode the injection and exhaust lines.

2. The combustion products need to be captured in order to be able to recycle them. For the combustion of hydrocarbon fuels, the formation of ash is undesired, but for metal fuels it is inevitable. This not only requires a system which will capture the ash, but might also cause issues when used as a fuel in a heat engine.

This property and requirement make it impossible to use metal fuels as a direct replacement for hydrocarbon fuels in conventional heat engines. Fortunately, there also are alternative methods which are briefly discussed below.

2.3.1 Wet cycle

In a wet cycle (metal-water reaction), the metal reacts with water which results in the production of hydrogen. This way, metals can function as hydrogen storage. The released hydrogen can be used in a fuel cell or burned directly. There are a few downsides or complications to this approach:

- Under normal conditions, a metal-water reaction is relatively slow. If a large power gener-

ation is desired, a large reaction speed is required. Some options to increase the reaction speed are: increasing the temperature, reacting with subcritical water or reducing the particle size of the metal [12].

- In correlation to the previous point, the metal fuel needs to be sealed properly to avoid non-wanted metal-water reactions. Not only would this render the fuel useless, but for large reactions speeds it could also cause explosions.

- For a wet cycle, water is required. This requirement will lead to a lower energy density of the total system. This is a problem mainly for transport and dry areas.

In order to effectively generate power using this method, control over the hydrogen production and efficient hydrogen to energy conversion are essential.

2.3.2 Internal Combustion Engine

Using solid fuels in internal combustion engines has been attempted numerous times, but rarely successfully. One of the main problems with solid particles is that a large surface-to-volume ratio (i.e. small particle sizes) is required in order to obtain the required reaction rate. This problem has been largely solved with technologies which can create tiny particles. However, research has shown that there is a limit to the effective particle size. At nano size the particles tend to agglomerate on dispersal [13].

In addition to the requirement of tiny particles, there are also practical problems when using solid fuels in internal combustion engines. Piriou, Vaitilingom, Veyssière, *et al.* provide an overview of past research on biomass fueled internal combustion engines in their paper [14]. They describe the main problems as:

- Difficult fuel metering due to non-uniformity of the powder and slowly blocking of the injection system.

- Engine wear due to the abrasive nature of the powder.

- In case of using coal powder as fuel: poor ignition control. The combustion process of solid fuels is more complicated than that of liquids or gases (e.g. drying, heating, devolatilization, volatiles combustion and char combustion have to be considered).

Metal is an inorganic material, which means that its composition is relatively constant compared to organic materials which will often contain impurities. This might imply that the combustion process could be more accurately predicted or modeled, such that the last problem might not apply to metal fuels. However, blocking of the injection system and more importantly engine wear can still be major problems when using metal-powder fuel in an internal combustion engine. Bergthorson, Goroshin, Soo, *et al.* also conclude that combusting metal-powder fuels in internal combustion engines is probably not realistic.

2.3.3 External Combustion Engine

External Combustion Engines based on the Rankine cycle are used globally in order to generate power. The used heat source is arbitrary (e.g. fossil fuels, solar power or nuclear power). These systems can be adapted to use metal fuels as their power source. Bergthorson, Goroshin, Soo, *et al.* propose a metal-fueled combustor for this purpose.

The most well-known external combustion cycles are the Rankine- (steam) and the Stirling cycle. Demirbas and Meydan have made a comparison of these two cycles with the usage of biomass as fuel in mind [15]. They describe the external combustion engines as extremely clean and efficient engines, but they describe a few disadvantages of the Rankine cycle:

- Due to a large exposed surface area, there is also a large heat loss.

- Maintaining streams at high temperatures is difficult.

- Because an engine based on the Rankine cycle has a low power-to-weight ratio, the required systems are bulky. This makes the steam engine less practical for usage in small vehicles, such as cars.

Both the Stirling as the Rankine cycle have one major disadvantage for non-continuous usage such as in vehicles: they have a fairly lengthy start-up time. In case of the Rankine cycle the developing of sufficient pressure through steam production takes some time. For Stirling engines the required temperature for normal operation is only achieved after a period of heating. Stirling engines also have a low power density. However, Nightingale has shown that a Stirling engine is usable for automotive purposes when using the right configuration [16].

2.3.4 Gas turbine

The most obvious solution to use a gas turbine with metal fuel would be to directly replace the gas stream by metal powder in air. This however will likely only be a theoretical solution, as impurities in a gas turbine will cause erosion. A stream of solid particles will inevitably damage the gas turbine.

The alternative is to use an Externally Fired Gas Turbine (EFGT). This is the turbine equivalent of an external combustion engine. The following section will explains the basics of an EFGT.

Externally fired gas turbine
In an EFGT, the gas inside the turbine is separated from the combustion. The heat of combustion is transferred to the working fluid by a heat exchanger. A high-temperture heat exchanger is required due to the high combustion temperatures. Compared to a directly fired gas turbine, the efficiency of an externally fired gas turbine will be lower. Figure 2.4 shows schematic overviews of a directly fired and an externally fired gas turbine.
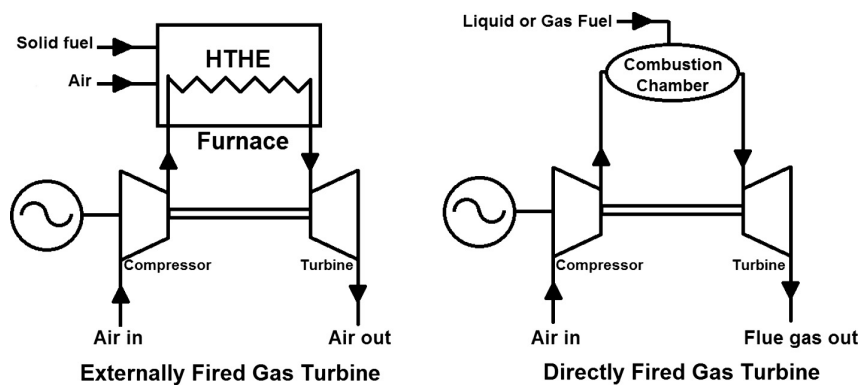
Figure 2.4: Schematic overviews of an externally and directly fired gas turbine. Reprinted from Al-attab and Zainal, "Externally fired gas turbine technology: A review" [17].

There are two main advantages to using external combustion in a turbine: 'dirty' fuels can be used for heating and the waste heat of the turbine can be used in a recuperative process [18]. Kautz and Hansen have made a comparison of the net-electric efficiency of most of the conventional technologies for burning biomass, as shown in Figure 2.5.
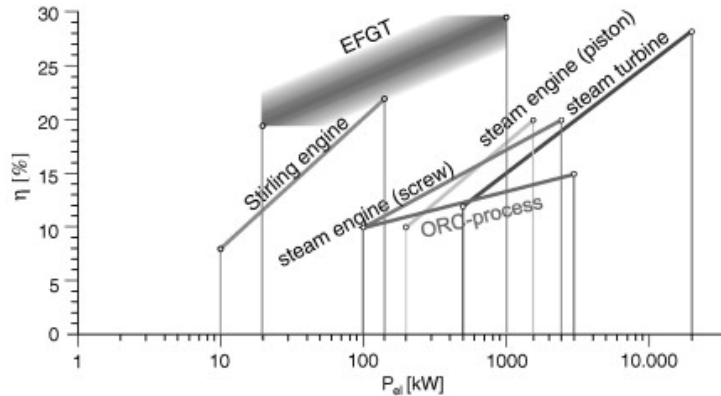
Figure 2.5: Typical unit size and efficiency of conventional technologies for combined heat and power plants burning biomass. Reprinted from Kautz and Hansen, "The externally-fired gas-turbine (EFGT-Cycle) for decentralized use of biomass" [18].

The figure shows than an EFGT can obtain a high efficiency over a broad power range. This makes it a viable alternative to a steam engine for example. Ferreira and Pilidis have made a comparison of the power and efficiency of a biomass fueled EFGT and a conventional turbine [19]. As they expected, the efficiency of an EFGT is lower than that of a conventional turbine (mainly due to the lower combustor efficiency). State-of-the-art heat exchangers would improve the efficiency, but Ferreira and Pilidis do not expect the first applications to have such technology. For that reason they have focused on more conservative technology.

Another method to increase the efficiency is by using a combined cycle, e.g. using the exhaust gas to power a steam turbine. This is one approach to increase the efficiency of the power generation, but a different method is to use a Combined Heat and Power (CHP) plant. By using a CHP device, no heat is lost as heating is one of the purposes of the device. The power efficiency might not be high, but the total efficiency will be because all energy will be used.

2.3.5 Microturbine

Gas turbines are usually operated on commercial scales of several hundred megawatts. For smaller scales, microturbines can be used. These usually operate in the range of 10 kW to 1 MW, but there is no theoretical limit to the generated power. However, the downsizing of a turbine leads to some complications.

The main problem is that the required blade tip speed in the turbine needs to be maintained. The blade tip speed is directly proportional to the diameter of the rotor. Thus decreasing the diameter will require larger rotational speeds to maintain equal blade tip speeds. For this reason, extreme rotational speeds are required for tiny turbines. High temperatures combined with large rotational speeds will inevitably cause problems in a small unit, which is one of the main challenges of developing microturbines.

The University of Leuven started to develop a micro gas turbine of 1 kW [20]. They describe the

main problems as the high required rotational speed, the high temperature and the efficiency of the components. At MIT they have taken it even further by developing a chip-sized micro turbine [21]. This system operates at extremely high rotational speeds of 20000 rotations per second. Peirs, Reynaerts, and Verplaetsen have developed a slightly larger microturbine wihch produces 28 W mechanical power with an efficiency of 18% [22].

The research of microturbines is typically performed on conventional gas turbines. Adding external combustion to the system will complicate it further, thus an externally fired microturbine is worth researching, but a working prototype may not be expected anytime soon.

2.3.6 Photovoltaics

Energy generation by photovoltaics is most commonly used in the field of solar power. A photovoltaic (or solar) cell converts the energy of light into electricity. A part of the energy generated by combustion of metal powder could be transformed into electricity by capturing the radiation of the flame on a photovoltaic cell. The spectrum of the emitted light has to match the spectral sensitivity of the photovoltaic cell in order to achieve a high efficiency. The fact that metal flames are highly radiative is the reason why a photovoltaic system is of interest when trying to harvest energy from a metal flame.

Photovoltaics might not seem to be the obvious choice for generating energy from flames. However, the technology is relatively simple and cheap. The next chapter will go into more detail on harvesting energy with photovoltaics.

3 Photovoltaics

This chapter will focus on energy production by photovoltaics. With this technology, light is converted into electricity by using semi-conducting materials which exhibit the photovoltaic effect. Photovoltaics is most commonly applied in solar panels.

This chapter will explain the basics of (electromagnetic) radiation and the requirements to convert radiation to electricity. The goal is to provide the necessary background information to understand why and how photovoltaics can be applied for energy harvesting from metal flames.

Firstly, it is explained why photovoltaics is researched as energy harvesting technique for metal fuel flames. Secondly, the concept of radiation is explained along with the different types of radiation. Finally, the theory behind photovoltaics is examined.

3.1 The benefits of photovoltaics

One might wonder why one would try to use photovoltaics to harvest the radiative energy of a flame. With regards to metal fuels, there are two ways to approach it: metal fuels as an alternative for fossil fuels, or metal fuels as an alternative for batteries.

In both of these approaches one would like to achieve a high efficiency. The efficiency of just a photovoltaic system will not be able to compete with existing technologies such as a fossil-fuel powered internal combustion engine. However, one of the advantages of photovoltaics is that it can be combined with a heat engine. One might look at electromagnetic energy as higher quality as compared to heat, as eventually all energy will be reduced to low temperature heat. By harvesting the electromagnetic energy, electricity can be produced directly and the leftover heat can still be used in a heat engine. Thus, a photovoltaic system can be considered as an addition to a heat engine, and not as a competitor.

When considering metal fuel as an alternative for a battery, the requirements change significantly. For example, a conventional lithium-ion battery has capacity of $\pm 140 \, \text{W h kg}^{-1}$. The gravimetric energy density of magnesium is $\pm 7 \, \text{kW h kg}^{-1}$ (Figure 2.1). This means that for an equal amount of energy per kilogram, an efficiency of $\pm 2 \, \%$ is required for the metal fuel system. This obviously is a simplification and does not consider all aspects of such a system, but it is clear that the desired efficiency is rather low. This means that in order to compete with a lithium-ion battery with regards solely to gravimetric energy density, an efficiency of 2 to 3 percent could be sufficient for a photovoltaic metal fuel system.

As explained above, the benefits of a photovoltaic system depends on the application. Firstly, it could be used as an addition to a heat engine to increase the overall efficiency. Secondly, a photovoltaic metal fuel system could be an alternative for a battery. Finally, a photovoltaic cell does not have any moving parts and its only requirement is proper (environmental) protection and a matching light spectrum.

3.2 Radiation

A definition of radiation is: 'emission or propagation of energy in the form of waves or particles'. The radiation that will be addressed in this report is electromagnetic radiation, in which the carrier of energy is a photon. Other forms of radiation are acoustic and gravitational radiation, which are not relevant for this research project. Electromagnetic radiation will simply be referred to as 'radiation' from here on.

Radiation is regarded in quantum theory as both a flow of particles (photons) as well as a wave. In this theory each photon has a specific energy, related to its wavelength as shown in Equation (3.1). A photon does not have any mass, so it can be regarded as a package of energy.

$$E_{ph} = \frac{h \cdot c}{\lambda} \tag{3.1}$$

In this Equation h is the Planck constant, c the speed of light and λ the wavelength. The relation between wavelength and frequency is $\lambda = \frac{c}{\nu}$.

The radiation with the highest energy is ionizing radiation with photon energies exceeding 1 MeV and wavelenghts of 1 pm. The lowest energy levels are described as extremely low frequency radiation with photon energies as little as 1 feV and wavelenghts up to 100 Mm.

Visible light is located between ultraviolet (UV) and infrared (IR) radiation and spans approximately the range of 380 nm to 750 nm, corresponding to energies of 3.26 eV to 1.65 eV.

3.2.1 Black body and gray body radiation

A black body is an idealized physical body that absorbs all of the incoming radiation, regardless of the wavelength or angle of incidence. A perfect black body has an emissivity (ϵ) equal to 1. A gray body will have an emissivity lower than one. This means that not all incident radiation is absorbed, but a portion of it is reflected or transmitted. In reality, perfect black bodies do not exist, and a gray body with an ϵ lower than one is usually considered.

The total power radiated per unit area from a gray body can be calculated with the Stefan-Boltzmann law, as shown in Equation (3.2).

$$I_e = \epsilon \sigma T^4 \tag{3.2}$$

Here I_e stands for the irradiance, ϵ for the emissivity, σ for the Stefan-Boltzmann constant and T for the temperature of the body.

As can be seen in this equation, the radiative power strongly depends on the temperature of the body. The spectrum of the radiation is defined by Planck's law, as shown in Equation (3.3).

$$B_\lambda\left(\lambda, T\right) = \frac{2hc^2}{\lambda^5}\epsilon\left(\lambda\right)\frac{1}{\exp\left(-\dfrac{hc}{\lambda k_B T}\right) - 1} \tag{3.3}$$

In this equation, B_λ stands for the spectral radiance and k_B for the Boltzmann constant. The peak of the radiance depends on the temperature of the body. The wavelength at which the peak is located can be calculated by Wien's displacement law [23], as shown in Equation (3.4).

$$\lambda_{max} = \frac{b}{T} = \frac{2.898 \times 10^{-3}\,\mathrm{m\,K}}{T} \tag{3.4}$$

Here, b is Wien's displacement constant.

The spectra of black bodies with temperatures of 1500, 2500 and 3000 Kelvin are plotted in Figure 3.1.
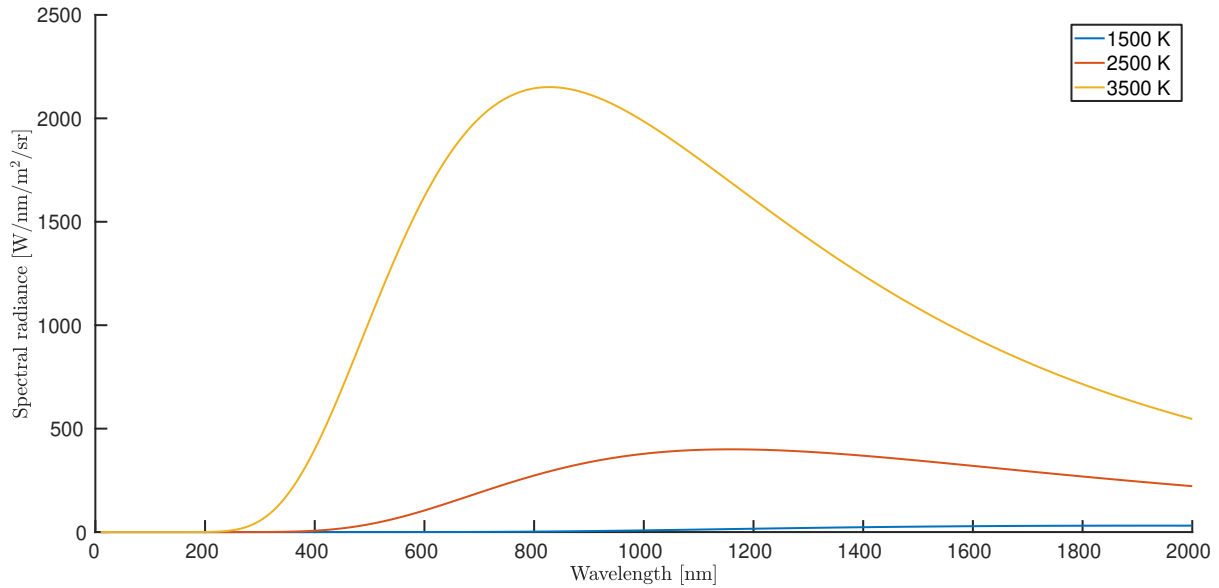
Figure 3.1: Black body spectra for bodies of 1500, 2500 and 3500 K. The strong dependence on temperature can be clearly seen. A body of 1500 K radiates mostly infrared and little visible light. For higher temperatures the amount of emitted visible light increases strongly.

The figure clearly shows the temperature dependence of the radiation. Also, for higher temperatures the peak shifts towards the range of visible light. A temperature of 1500 K is in the range of a candle flame, 2500 K is in the range of the flame temperature of iron powder and 3500 K is comparable to the flame temperature of aluminium powder. The spectra show that the higher temperatures of metal powder flames make them much more suitable for photovoltaics than other flames.

3.2.2 Molecular emission

Individual molecules have an internal energy which can take on specific, discrete values. Light emission or absorption of a molecule corresponds to a change in the internal energy of a molecule, as shown in Equation (3.5).

$$E_{after} = E_{before} \pm E_{ph} \tag{3.5}$$

Since the molecular internal energy can only take on discrete values, the photon energy is also discrete. The implies that only photons with a specific energy can be emitted or absorbed by a molecule.

A molecule can be described as a multi-particle system, which contains multiple degrees of freedom: electronic energy, internal vibrations and rigid rotations. These degrees of freedom are related to the internal energy of a molecule, as shown in Equation (3.6).

$$E_{internal} = E_e + E_v + E_r \tag{3.6}$$

Each of the terms shown in the equation can be modeled such that the internal energy of the molecule can be calculated as a function of its quantum state. This however is beyond the scope of this project. To understand why this is relevant, it is necessary to know that the average

number of molecules in a particular energy state is a function of temperature. If a molecule in a higher energy state transitions to a lower energy state, spontaneous emission will occur and a photon equal to the energy difference of the two states will be emitted. Thus, depending on the molecular species, radiation is not only generated by black body radiation, but also by molecular emissions. This molecular emission will be visible by distinct spectral lines.

3.3 Photovoltaics theory

The conversion of photons into electricity takes place in a semiconducting material. This process can be explained with the band theory of solids. This theory describes the available energies for electrons in a material. Instead of having discrete energies as when describing a free atom, the available energy states can be described by bands: the valence and conduction band. The bands are illustrated in Figure 3.2.
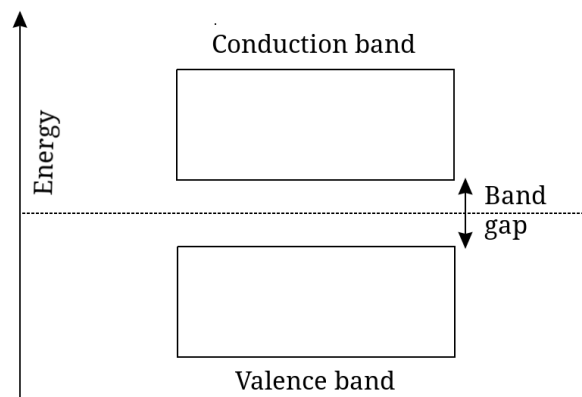
Figure 3.2: Illustration of the energy bands of a solid. The bands are visualized for a semiconductor, i.e. there is a small bandgap. An insulator would have a large bandgap whereas a conductor would have overlapping bands.

As shown in the figure, the two bands are separated by a small gap: the bandgap. If an electron wants to travel from the valence to the conduction band, it requires the energy visualized by the bandgap to do so. At $0\,\mathrm{K}$, all the electrons are located in the valence band and are unable to travel to the conduction band. At room temperature however, electrons are able to travel to the conduction band, which generates a negative charge in the conduction band and a positive charge in the valence band (a lack of electrons, also called a hole). By addition of specific impurities (called doping), the conduction can be enhanced thus making the travel between bands easier. At room temperature, the material of the impurity (e.g. phosphorus or boron) is ionized which means that it can donate or accept electrons from the semiconducting material. This generates a positive or negative charge in the semiconducting material.

By carefully selecting the impurity type and concentration, a p-n junction can be created as shown in Figure 3.3.
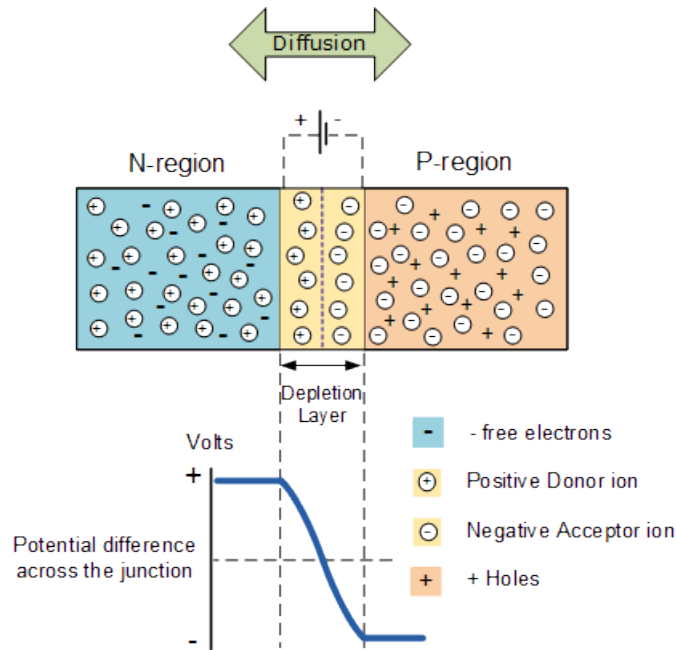
Figure 3.3: Illustration of a p-n junction. The left hand side is negatively charged whereas the right hand side is positively charged. In the depletion layer electrons from the n-region travel to the p-region, leaving behind positively charged ions. At the p-region, the electrons are accepted by the holes leaving behind negatively charged ions. The charge difference in the depletion layer creates a strong electric field. Reprinted from *Pn junction theory*, http://www.electronics-tutorials.ws/diode/diode_2.html, Accessed: 11-4-2017.

As shown in the figure, an electric field is generated in the depletion layer (also called space charge region). When a photon (with an energy larger than the required bandgap) hits the semiconductor, it will move one electron from the valence to the conduction band. If this electron is generated close to the p-n junction, it will be separated by the strong electrical field in the depletion layer, leaving behind a hole. An electron which is created deeper into the p-region can travel towards the depletion layer by diffusion. Electrons in the n-region are collected by the contact grid and travel to the back contact through the external load. This process is illustrated in Figure 3.4.
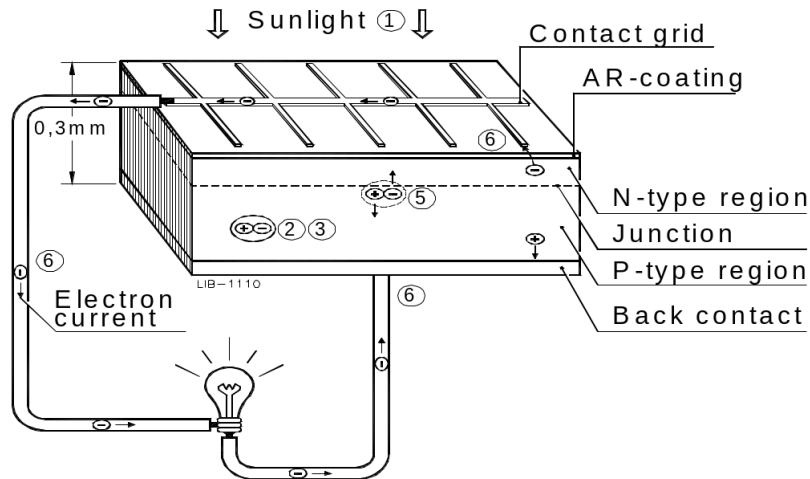
Figure 3.4: Illustration of the structure and working principle of a solar cell. On impact, a photon frees an electron, which is then separated from the hole by the p-n junction. The electron travels from the n-region through the external load back to the p-region, thereby generating a current. Reprinted from *Lecture notes of 4se00 - sustainable energy sources*, 2015.

As described before, a photon with an energy larger than the required bandgap will free an electron. This implies two sources of energy loss:

1. Photons with an energy smaller than the required energy will not generate an electron-hole pair.

2. Photons with an energy larger than the required energy will have its excess energy converted to heat.

Furthermore, a generated electron can also recombine with a formed hole. This also is a source of energy loss. These three phenomena add up to an energy loss of approximately 68% for a silicon solar cell [25].

These losses imply that it is important to choose the right semiconducting material that matches the incoming spectrum. The solar spectrum is well defined, and initial calculations on the achievable efficiency were performed by Shockley and Queisser in 1961 [26]. Based on their research, Rühle has defined the maximum achievable efficiency of a single junction solar cell at 33.7% with a bandgap of 1.34 eV [27]. The bandgaps of some of the most commonly used semiconducting materials are shown in Table 3.1 (approximates because the bandgap is temperature dependent).

The reason that silicon is the most commonly used material in solar photovoltaics is that its bandgap is relatively close to the bandgap of peak efficiency as calculated by Shockley and Queisser. Furthermore, silicon is one of the most abundant materials on earth which keeps the costs relatively low. In space applications, where costs are less of a concern, Gallium Arsenide is often used because it has a higher efficiency.

The efficiency (and spectral mismatch) of a silicon cell for the AM1.5 solar spectrum (i.e. the light travels 1.5 times the shortest possible path to earth, the zenith) is illustrated in Figure 3.5.

Table 3.1: Approximate bandgaps of some of the most commonly used semiconducting materials. Only a small selection is shown. There are many more semiconducting materials, however most of them have a high bandgap which makes them unusable for photovoltaics.

Material	Acronym	Bandgap [eV]
Gallium Arsenide	GaAs	1.42
Silicon	Si	1.12
Germanium	Ge	0.66
Gallium Antimonide	GaSb	0.72
Indium Gallium Arsenide	InGaAs	0.36 - 1.42
Indium Gallium Arsenide Antimonide	InGaAsSb	0.29-0.72
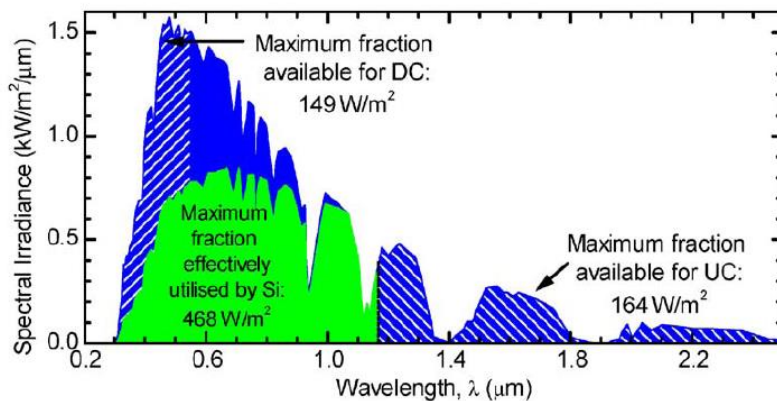
Figure 3.5: Illustration of the spectral mismatch of the solar spectrum for a silicon photovoltaic cell. The bandgap of a silicon semiconductor is approximately 1.12 eV, which corresponds to a wavelength of 1088 nm. The blue graph shows the incoming irradiance from the sun and the green graph shows the amount of irradiance which is converted in a silicon solar cell. The figure shows that photons with a longer wavelength are not absorbed at all, and the energy of photons with a shorter wavelength is only partially absorbed. The figure also shows the fractions available for up and down conversion (UC and DC), i.e. splitting or combining the energy of photons to generate photons which can be effectively absorbed. Reprinted from *Lecture notes of 4se00 - sustainable energy sources*, 2015.

3.4 Single- and multi-junction cells

As explained in the previous section, the maximum efficiency for a single-junction solar cell is 33.7%. To work around this efficiency limit, multiple photovoltaic cells can be used which each absorb a different part of the solar spectrum. The most commonly used setup is having multiple photovoltaic cells stacked on top of each other. The top cell has the highest bandgap. Photons with a sufficiently high energy are absorbed by the cell, and photons with a lower energy are transmitted. The next cell has a lower bandgap to capture the transmitted photons with a lower energy.

A multi-junction cell can be connected either in series or in parallel. Cells which are connected in series should have a matching photocurrent in each cell to minimize losses (the current is limited to the lowest photocurrent for cells which are connected in series). A solution to this problem

would be to connect the cells in parallel, however the production of such a cell is challenging [28]. It requires a transparent and conductive layer as a common electrode. Such cells have been fabricated, but Etxebarria, Furlan, Ajuria, *et al.* conclude that the lower efficiency and more difficult manufacturing process make them non-suitable for development of solar modules.

3.5 Maximum power point

The power generated by a photovoltaic cell depends on the resistance attached to the cell. By varying this resistance, a current-voltage curve can be created. The current will vary from the short-circuit current I_{sc} to zero while the voltage will vary from zero to the open-circuit voltage V_{oc}. The voltage and current can be plotted in an I-V curve, as shown in Figure 3.6.
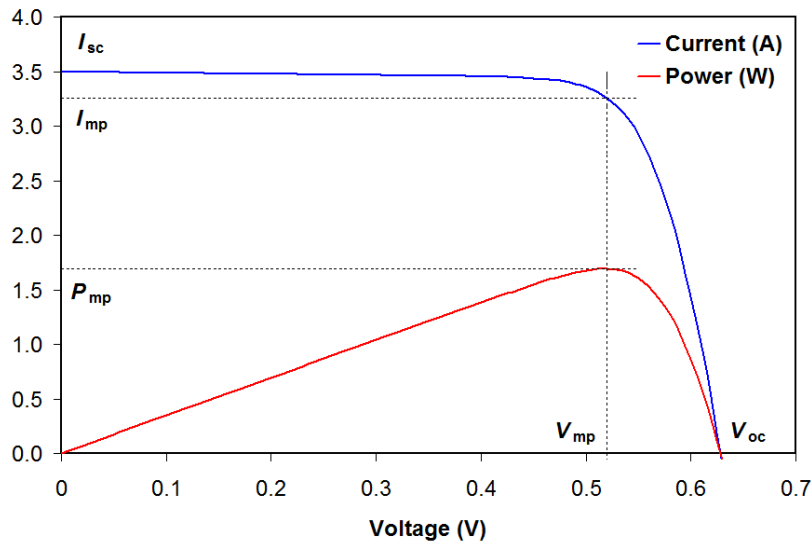
Figure 3.6: Example of an I-V curve of a photovoltaic cell. The power curve is also plotted. The voltage varies between zero and V_{oc} whereas the current varies between I_{sc} and zero. There is a single point on the curve where the produced power is maximized: the point of maximum power P_{mp}.

As the I-V curve depends on the irradiance, it is necessary to properly adjust the resistance when the light source changes. As can be seen in the figure, the point of maximum power is located at approximately 80% of V_{oc}. When the light source changes, the I-V curve also changes. In order to remain at the point of maximum power, different methods can be used. Two of the most commonly used methods are briefly described below.

- Perturb-and-observe. The operating voltage of the PV cell is perturbed by a small increment. This change in operating voltage is accompanied by a change in power: ΔP. The sign of ΔP determines if the operating point moved towards or away from the point of maximum power. By repeating this procedure (in the right direction) the point of maximum power can be tracked.

- Constant voltage. As can be seen in Figure 3.6, the point of maximum power is located at a constant fraction of V_{oc}:

$$V_{mp} = k \cdot V_{oc} \tag{3.7}$$

In which k is a constant smaller than 1. This is the simplest method, but the value of k might vary under different temperature and irradiance which means that it is less accurate.

Hohm and Ropp compared the efficiencies of the above methods and concluded that perturb-and-observe (97.8% overall efficiency) is more efficient than constant voltage (91.2% overall efficiency) [29]. More efficient and complicated methods also exist, but they are beyond the scope of this research project. One should remember that a PV cell will not automatically function at maximum power, but effort is required to achieve this.

3.6 Thermophotovoltaics

Thermophotovoltaics is a method of converting heat directly into electricity. By heating an emitter to the required temperature, it will start to radiate. The radiation from the emitter is captured on a photovoltaic cell which in turn produces electricity. There are two major advantages to this approach. Firstly, any heat source can be used which means that thermophotovoltaics can be applied for a broad range of purposes. Secondly, the efficiency can be increased by control of the absorbed spectrum (in contrast to solar photovoltaics, which always has the same spectrum) [23]. The main disadvantage with conventional thermophotovoltaics is the relatively low achievable temperature of the emitter. The achievable temperature is typically up to $\pm 2000\,\mathrm{K}$, which is much lower than the black body temperature of solar radiation ($\pm 5800\,\mathrm{K}$). This results in mostly infrared radiation which in turn requires semi-conducting materials with a low bandgap. Some of the most commonly used low-bandgap materials are also listed in Table 3.1.

3.6.1 Reflector

Another advantage of thermophotovoltaics is that a reflector can be used to reflect non-absorbed photons back to the emitter. By doing this, the energy contained in the photon is not lost, but used to reheat the emitter. In the ideal case this means that 100% of the energy is converted to photons. The reflector can be applied in two ways: the photons can be filtered before it reaches the PV cell or the unused photons can be reflected by the PV cell. A thermophotovoltaic cell of high quality will reflect the radiation which is not converted to electricity.

3.6.2 Applicability for metal fuels

Essentially, thermophotovoltaics covers what is required to retrieve radiative energy from a metal flame. Bauer concludes that direct conversion of the radiation of a flame (without an emitter) is often unsuitable for thermophotovoltaics because of the relatively low radiative energy fraction, an unsuitable radiation spectrum and fouling aspects [23]. By choosing the proper photovoltaic cell (e.g. gallium antimonide) however, direct conversion from flame radiation to electricity is possible [30].

However, when using a metal flame, there are a few major differences when using thermophotovoltaics.

- The combustion temperature of metal powders is much higher than the maximum achievable temperature for emitters. This will result in radiation of larger power, of which a large fraction is located in the visible spectrum. In turn, this makes it possible to use photovoltaic cells with a relatively high bandgap for thermophotovoltaics, such as silicon. By using Wien's displacement law (Equation (3.4)), the peak of the radiative spectrum can be calculated. For example, for aluminium with a flame temperature of $3541\,\mathrm{K}$ [1], this gives a peak at $810\,\mathrm{nm}$ or $1.53\,\mathrm{eV}$.

Bouzid and Dehimi concluded that the ideal black body emitter temperature for a thermophotovoltaic system based on a gallium antimonide (GaSb) cell is 2200 K [31]. This is also approximately the flame temperature of iron powder. This might mean that for iron combustion, the maximum efficiency can be reached by using only one type of semiconductor (GaSb). For metals with a higher flame temperature, a multi-junction photovoltaic cell might be required to reach the maximum efficiency.

- While the radiating species in a metal powder flame are in fact solid bodies, it is a flow in which these particles are located. Thus, in order to apply filters, optics or reflectors, a stable flow and flame are necessary.

- In contrast to 'dirty' hydrocarbon fuels, if the produced metal-oxide particles are effectively captured after combustion of the metal powder, there is little fouling. For long-term use of a thermophotovoltaic system it is essential that the optics or photovoltaic cells will not be contaminated, as this will reduce the radiative energy that can be captured.

As explained in Section 3.4, a photovoltaic cell can be either a single- or multi-junction configuration. Multi-junction solar cells offer the highest efficiency, but they might not be usable for thermophotovoltaics. Because the multi-junctions cells are usually connected in series, it requires a constant and defined light source to reach the maximum efficiency. As these cells are usually designed for the solar spectrum, the efficiency when using the radiation of a metal powder flame might be much lower, or it might not even work at all. In order to use a multi-junction photovoltaic cell, the spectra of the metal powder flames first need to be measured. When the flame spectrum is known, a multi-junction cell can be selected or designed which exactly matches this spectrum. However, this also requires that the spectrum is constant at all times to maximize the efficiency.

In order to find the right materials, setup and efficiency for photovoltaic energy harvesting from metal flames, it is required to first characterize the flame and radiation.

4 Photovoltaic energy generation

The previous chapters provided the necessary background information about metal fuels and photovoltaics. In this chapter these two will be combined in order to reach the goal: produce energy from a metal flame by means of photovoltaics.

This chapter aims to describe the used methods for characterizing the metal flame radiation. Furthermore, a method to calculate the efficiency of a photovoltaic system when using a metal flame is examined.

To achieve this, the first part of this chapter will focus on defining the spectrum and power of metal flames; magnesium flames in particular. Furthermore, it is described how the overall efficiency of a photovoltaic system can be calculated.

4.1 Flame characterization

4.1.1 Angular distribution of flame radiation

The radiation of a flame is not equal in all directions [2]. Because only a fraction of the radiation is actually measured during a measurement, the distribution of the radiation of the flame as function of the polar angle needs to be determined.

In order to measure the angular distribution of the flame radiation, diffuse white ping pong balls were placed on a mount at a fixed radius with a 10 degrees interval. It is assumed that there is diffuse reflection from the surface of the ping pong balls. All balls are equivalently arranged with respect to the flame and the camera. This means that the intensity of the image of all corresponding points of the balls will be proportional to the illumination intensity. This intensity is defined by the intensity of the flame radiation in the direction of the corresponding ball. This, in particular, is valid for the points on the ball surface where the image intensity has a local maximum. Thus, by finding the maximum image intensity for every ball with respect to its angular position, the angular distribution of the flame radiation can be determined.

By making a photograph with a Grasshopper3 (GS3-U3-123S6C-C) camera of the mount while a sample is burned, the angular distribution of the radiation can be calculated in MATLAB. The used setup is shown in Figure 4.1. The used script for analyzing the results is shown in Appendix A.
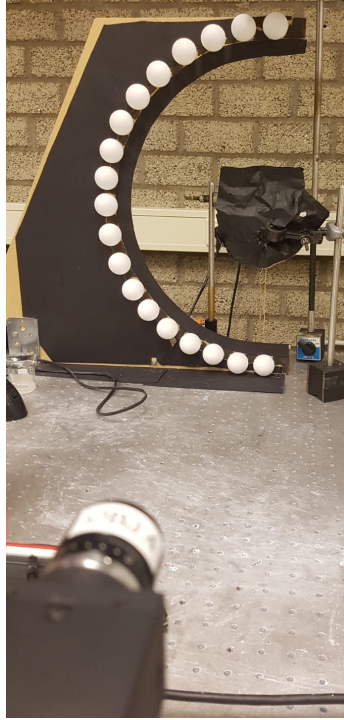
Figure 4.1: Setup for the measurement of the angular distribution of the radiation of a flame. The ping pong balls are placed with a 10 degrees interval at a fixed radius from the center. The flame will be located in the center of the ring. From the resulting photograph, the angular distribution of the radiation of the flame can be calculated.

The result is expected to resemble the graph shown in Figure 4.2, as measured by Shoshin and Altman.
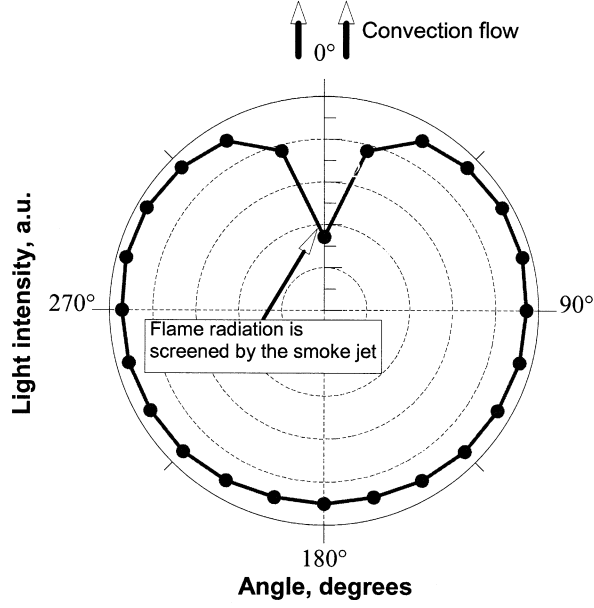
Figure 4.2: Angular distribution of the radiation of a single particle magnesium flame. Reprinted from Shoshin and Altman, "Integral Radiation Energy Loss During Single Mg Particle Combustion" [2].

Isotropy of radiation

The angular distribution is measured as a function of the polar angle θ. If the total radiation of the flame is considered, the result needs to be integrated across the azimuthal angle ϕ. Because the circumference of a sphere at height h is smaller than the circumference at the base, the top and bottom of the sphere have a smaller effect on the total radiation.

As the radius at height h is equal to $R \sin \theta$ (shown in Figure 4.3), the radiated area of the sphere at that height is equal to $2\pi R \sin \theta$. The isotropy of the flame is calculated by multiplying the intensity at each location i by the illuminated area, and dividing that result by the intensity at $\theta = 90°$ multiplied by the total illuminated area, as shown in Equation (4.1). Because the contribution at zero and 180 degrees will be neglected this way, the average between two neighboring points is used for the calculation. $N = 19$ is the number of measurement points.

$$k = \frac{\sum_{i=1}^{N-1} \frac{I_i + I_{i+1}}{2} 2\pi R \sin\left(\frac{\theta_i + \theta_{i+1}}{2}\right)}{I_{\theta=90°} \sum_{i=1}^{N-1} 2\pi R \sin\left(\frac{\theta_i + \theta_{i+1}}{2}\right)} = \frac{\sum_{i=1}^{N-1} \frac{I_i + I_{i+1}}{2} \sin\left(\frac{\theta_i + \theta_{i+1}}{2}\right)}{I_{\theta=90°} \sum_{i=1}^{N-1} \sin\left(\frac{\theta_i + \theta_{i+1}}{2}\right)} \quad (4.1)$$

I_i is the pixel intensity at polar angle θ_i.
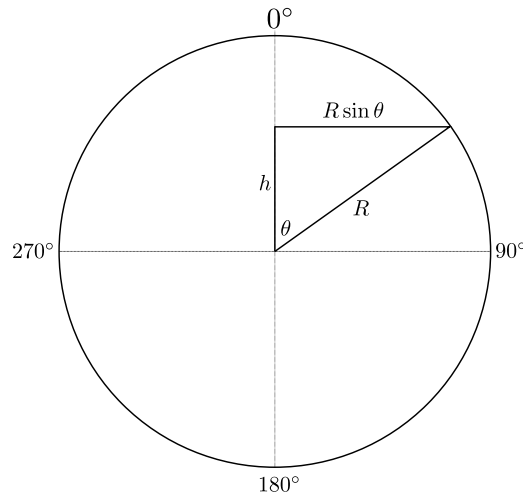
Figure 4.3: Visualization of the radius at height h in polar coordinates.

4.1.2 Radiated energy

Laser power meter

A laser power meter is used to measure the radiative energy that is released upon the combustion of a metal particle.

A laser power meter is a simple device which uses a thermopile sensor, an absorbing disk and a cooling body. A laser beam is directed onto the absorbing disk and its power is absorbed and converted to heat. The heat flows radially through the thermopile and dissipates on the periphery. The thermopile sensor generates a signal proportional to the temperature gradient between the inner and outer side. This gradient depends on the heat flow which is generated by absorption of the laser beam. As the temperature difference defines the generated signal, the measurement is not dependent on the ambient temperature.

Figure 4.4 shows an illustration of a thermopile sensor.
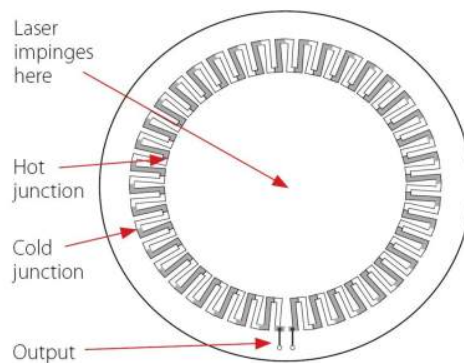
Figure 4.4: Illustration of a thermopile sensor. The laser beam is pointed at the center of the circle of hot junctions. When the laser beam is absorbed, the temperature increases locally and the heat flows through the thermocouples. With the temperature gradient across the thermocouples, the power of the laser beam can be calculated. Reprinted from https://www.newport.com/t/thermopile-laser-power-sensor-technology.

However, as the name states, laser power meters are normally used for measuring the power of laser beams. There are some important differences between a laser beam and the radiation of a (metal) flame. First of all, a laser beam consists of a single wavelength in contrast to a flame which consists of a spectrum of wavelengths. A laser power meter is developed to measure the power at a defined wavelength. In order to accurately measure the power of a flame, the spectral response of the laser power meter needs to be flat along the measured spectrum. Secondly, the response time of a laser power meter is relatively slow. Typical response times are in the order of seconds. For this reason, it is not possible to measure the power of a variable source instantaneously.

Fortunately, the main point of interest is the total energy radiated by a combusted metal fuel sample. It needs to be verified that the laser power meter can measure the total radiative energy. This means that integration of the power signal should result in the total energy emitted by a sample.

According to the working principle of a laser power meter, the signal at each moment is proportional to the thermal gradient on the absorbing disk. This gradient, in turn, is proportional to the local heat flux. Thus, it can be suggested, that the integral of the signal produced by a radiation pulse taken over the whole time period when this signal is non-zero (e.g. until all absorbed heat has flown from the hot to cold side in the absorbing disk), will be proportional to total absorbed energy of the pulse, regardless of the pulse duration and variation in power.

In order to verify this, the setup shown in Figure 4.5 was used.
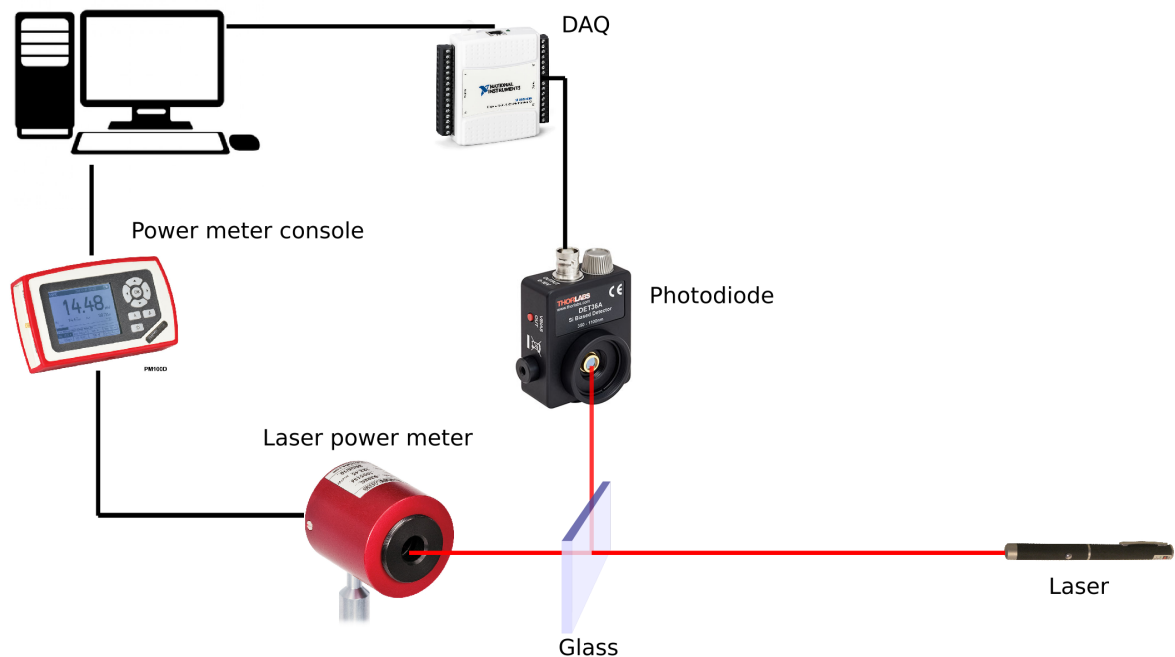

Figure 4.5: Experimental setup for the verification of the total energy measured by the laser power meter. A laser beam is split using a shard of glass and pointed on both the laser power meter as well as the photodiode. Laser pulses are generated by blocking the light in front of the laser. The pulse time is measured by the photodiode and the power is measured by the laser power meter.

The source needed to be a laser of constant power. A direct-current powered laser pen showed less fluctuations in power than an alternating-current powered laser. For that reason, a laser pen was used as source. A fraction of the laser beam was split of the main beam by using a shard of glass. By blocking the light, pulses of durations varying from ≈ 0.1 to ≈ 10 seconds were created. The pulse time was accurately measured by the photodiode, and the power was measured by the laser power meter.

It is important that the measurement time is sufficiently long to enable the laser power meter to cool down after the pulse. This way, the length of the pulse is provided by the photodiode signal and the total energy of the pulse can be calculated by integrating the power signal.

To be able to use the laser power meter to measure the radiative energy of a combusted metal sample, it needs to be verified that there is a linear dependence with time: $E = P \cdot t$.

The laser power meter that has been used is the Thorlabs S302C. The main reason for choosing this laser power meter is that it is thermally stabilized, meaning that temperature of its body is constant during measurements and calibration of the laser power meter performed before the measurement remains valid during total duration of the pulse. Another reason is that the response of the laser power meter is flat across a broad wavelength range, as shown in Figure 4.6.
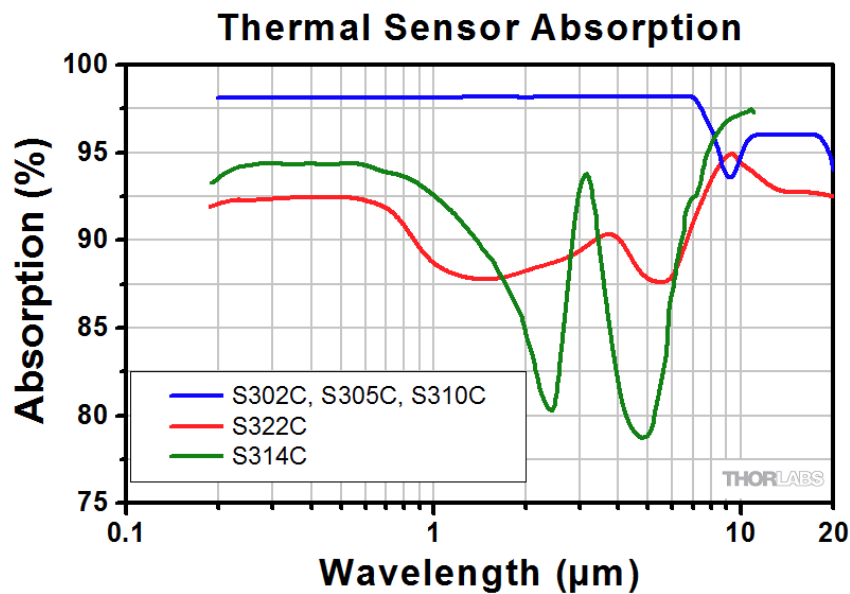
Figure 4.6: Thermal sensor absorption of the S302C laser power meter. It can be seen that the response is flat across a wavelength range of $0.2\,\mu m$ to $7\,\mu m$, which covers both the visible as well as the infrared range. Reprinted from the website of Thorlabs.

The results of the experiment described above are shown in Appendix B. From the results it can be concluded that the laser power meter can be used to accurately measure the radiated energy of a flame.

Measuring the power of a flame

The laser power meter was placed next to a magnesium sample at a defined distance r and carefully aligned. With the assumption that the magnesium sample radiates like a point source, the solid angle occupied by the laser power meter, Ω can be calculated with Equation (4.2).

$$\Omega = \frac{A}{r^2} \tag{4.2}$$

The area A in this case is defined by the precision aperture (Appendix C). The total solid angle of a sphere is equal to $4\pi\,\mathrm{sr}$.

The measured power signal was integrated over time to obtain the energy radiated by the sample on the laser power meter. The total radiated energy was calculated by integrating the measured solid angle over the total solid angle, and multiplying by the isotropy factor k, as shown in Equation (4.3).

$$E_{rad} = kE_{meas}\frac{\Omega_{tot}}{\Omega_{aperture}} \tag{4.3}$$

The total energy contained in the sample was calculated by assuming that the complete sample is converted to magnesium oxide upon combustion:

$$2\,\mathrm{Mg} + \mathrm{O_2} \longrightarrow 2\,\mathrm{MgO}$$

The enthalpy of formation, ΔH_f, of magnesium oxide is $-601.6\,\mathrm{kJ\,mol^{-1}}$ [32]. By calculating the number of moles of magnesium in the sample and multiplying this with the enthalpy of formation, the total energy contained in the sample is obtained.

Finally, by dividing the radiated energy by the total energy contained in the sample, the fraction of radiated energy is calculated. The resulting efficiency is expected to be approximately 40% as measured by Shoshin and Altman [2], although a higher efficiency will obviously be appreciated.
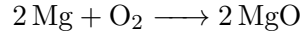
4.1.3 Spectrum

The spectrum of a flame was measured with a spectrometer. Spectrometers are available for different wavelength ranges. In this research project, the focus will be on radiation in the visible range. For that reason, the Ocean Optics USB4000 spectrometer with a wavelength range of $200\,\mathrm{\mu m}$ to $850\,\mathrm{\mu m}$ has been used for measurements.

The spectrometer was calibrated for absolute irradiance using a Ocean Optics HL-3P-CAL-EXT light source. This calibration enables the spectrometer to measure the spectral irradiance in $\mathrm{W\,m^{-2}\,nm^{-1}}$. By using the calibrated spectrometer, the power in the visible range can be measured, but more importantly the relative irradiance of the acquired spectra will be correct.

By integrating the spectral irradiance of the spectra with respect to the wavelength, the irradiance is obtained. Multiplying the irradiance by the surface area of the probe and integrating with respect to time will result in the energy in the wavelength range of the spectrometer (approximately the visible range), as shown in Equation (4.4).

$$E_{vis} = \int \left(A_{probe} \int I_{e,\lambda}\,\mathrm{d}\lambda \right) \mathrm{d}t \tag{4.4}$$

The energy in the visible range as fraction of the total radiated energy is obtained by dividing E_{vis} by E_{rad}.

In order to ease the measurements of the spectra, a new program has been written in MATLAB, as shown in Appendix D. For the processing of the results, multiple scripts have also been written which are shown in Appendix E.

Black body temperature
As explained in Section 3.2.1, a black body of a certain temperature will radiate according to Planck's law (Equation (3.3)). A radiating hot surface with a constant emissivity (i.e. a gray body) will radiate according to the same law, but with a lower intensity. By assuming a constant emissivity, Planck's law can be used to calculate the black body temperature of the acquired spectra. The optimization toolbox of MATLAB has been used to create a curve fit of the data with Planck's law. The variables of the function are T and a scaling constant. The curve fit will provide the black body temperature which has the best match for the acquired spectrum. The resulting black body temperature can be used to extend the acquired spectrum from the spectrometer. This way, a spectrum into the far infrared range can be extrapolated and the amount of radiation in the visible and infrared spectrum can be compared with the results of the measurement. This way, the assumption of a magnesium flame radiating as a gray body can be verified. The used MATLAB scripts are shown in Appendix F.

4.2 Photovoltaic energy harvesting

4.2.1 Spectral mismatch

Spectral mismatch is the difference between the available energy in a spectrum and the energy which can be absorbed by a photovoltaic cell. According to Equation (3.1), the energy of a photon depends on the wavelength. This means that the total energy in a spectrum is spread out over different energy levels. As explained in Section 3.3, photons with an energy higher than the bandgap are only partially converted and photons with a lower energy are not converted to electricity at all.

The difference between the available and absorbed energy can be calculated by converting the spectral irradiance to photon flux, Φ_p, as shown in Equation (4.5).

$$\Phi_p = \frac{I_{e,\lambda}}{E_{ph}} \tag{4.5}$$

The absorbed energy can now be calculated by multiplying the photon flux by the energy absorbed from each photon (the bandgap). Photons with a lower energy than the bandgap are not absorbed at all.

The MATLAB scripts used to calculate the spectral mismatch are shown in Appendix G.

5 Results

The previous chapter described the methods that have been used for the experimental measurements. In this chapter the obtained experimental results are shown.

The goal of this chapter is to provide a clear and consistent overview of the experimental results. This should enable the reader to verify or reproduce them.

First, a brief verification of the used methods and equipment is provided. Second, the results of the characterization of a magnesium flame are shown. Finally, the achievable efficiency in combination with a photovoltaic system is calculated.

5.1 Verification

5.1.1 Absolute irradiance

As explained in Chapter 4, both the laser power meter as well as the spectrometer are able to measure the power of a flame. The spectrometer will measure spectral irradiance whereas the laser power meter will measure irradiance.

If the entire emission spectrum of a light source is within the operating spectral range of the spectrometer, integration of the spectral irradiance with respect to wavelength should yield the irradiance. Thus, when measuring the same light source, the laser power meter and spectrometer should measure the same irradiance. The sensitive range of the spectrometer is much smaller than that of the laser power meter. In order to verify that they measure the same irradiance, a light source which only produces light within the range of the spectrometer is required. Fortunately, the spectrometer is designed to measure visible light which is exactly what most light emitting diodes (LED) produce.

The measured light source is a flashlight with a Cree XM-L Cool White (5000 K) LED. The spectrum of the LED is shown in Figure 5.1.
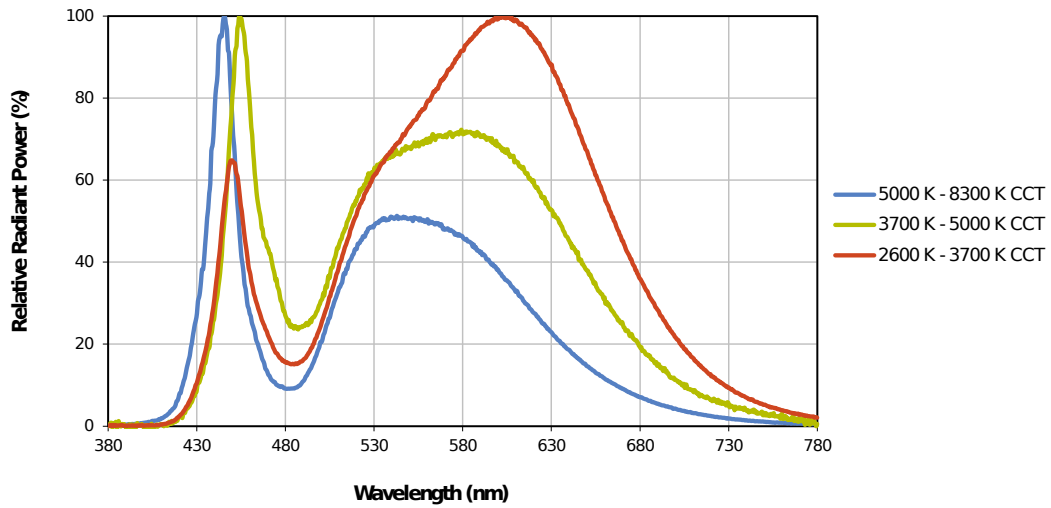
Figure 5.1: Relative irradiance spectrum of the XM-L LED. The used LED is the 5000 K variant. The produced light of the LED is clearly within the sensitive range of the spectrometer. Reprinted from *Cree xlamp xm-l data sheet*, http://www.cree.com/led-components/media/documents/XLampXML.pdf, Accessed: 30-10-2017.

It can be seen in the figure that the emitted light is well within the sensitive range of the spectrometer (200 nm to 850 nm).

The spectrometer has been calibrated as explained in Appendix E. Subsequently, the laser power meter and spectrometer were placed at the same position with regards to the light source one after another. The spectrum and power of the light source were measured. The results are plotted in Figure 5.2.
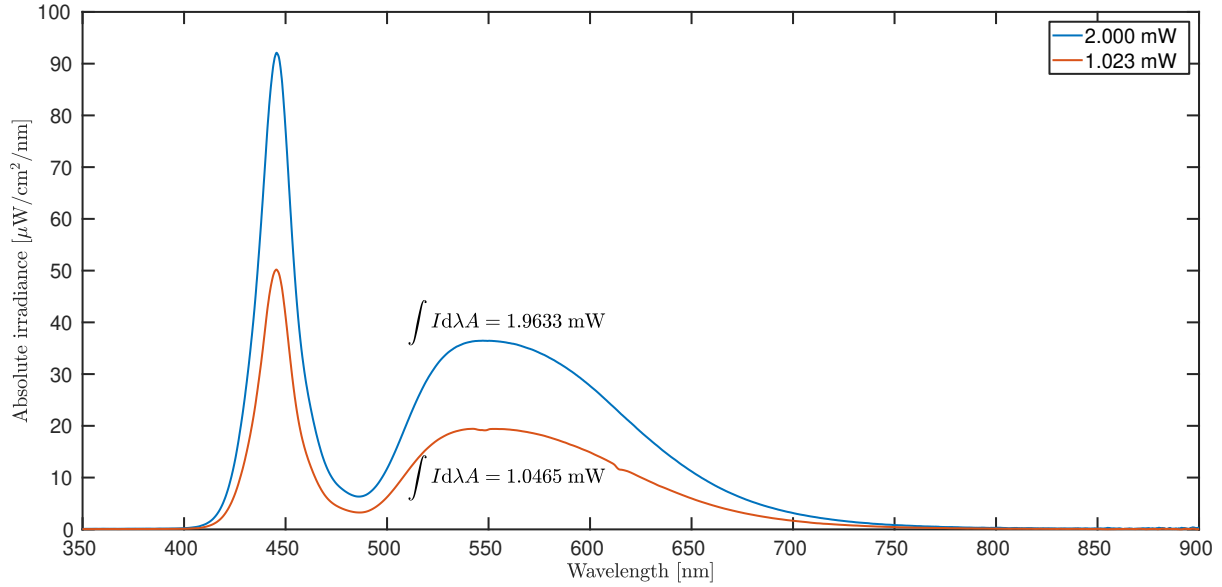
Figure 5.2: Comparison of the absolute irradiance as measured by the laser power meter and spectrometer. The spectrum measured by the spectrometer is plotted. The corresponding label shows the power as measured by the laser power meter. The total power measured by the spectrometer (the integral of the curve multiplied by the collection area) is also shown in the figure.

As can be seen in the figure, the measured power in both devices is similar. The measurement uncertainty of both devices is approximately 3% [34] [35]. The measured deviations are 1.9% and 2.3%, which are well within the expected range.

Thus, it can be concluded that both devices are able to correctly measure absolute irradiance with an accuracy as provided by their specifications.

5.2 Flame characterization

In order to analyze and characterize a magnesium flame, multiple different types of magnesium have been used. The first one is magnesium ribbon of 99.95 % purity with a thickness of 0.2 mm. The second is magnesium wire of ±95 % purity with a diameter of 2.4 mm. Finally, magnesium wire of 99.95 % purity with a diameter of 3 mm has been used.

The larger samples were mounted by wrapping and clamping them in a tungsten wire. This method of mounting could possibly affect the obtained results. To minimize this effect, small cylindrical samples of 3 mm were also made of the pure magnesium wire. A small hole was drilled in these samples. This allowed to mount them on a vertical 100 µm thoriated tungsten wire. The mounting methods are shown in Figure 5.3.

(a) Tungsten wire.

(b) Thoriated tungsten wire
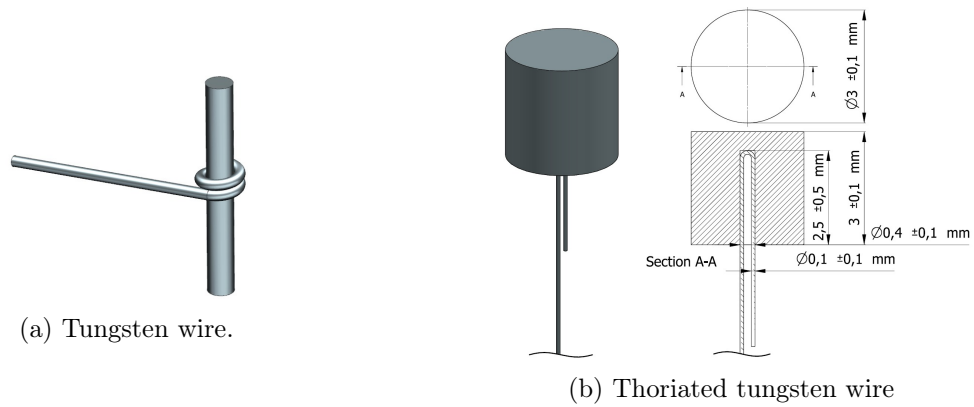
Figure 5.3: The methods used for mounting the magnesium samples. As clamping the samples in a tungsten wire seemed to affect the measurements, the smaller samples were placed on a thin vertical thoriated tungsten wire. Reprinted from Hoek, "The shining power of metal flames" [36].

5.2.1 Angular distribution of the flame radiation

The camera was set to record raw, uncompressed images with a bit depth of 16 bit. The gain was kept at zero and the shutter time was adjusted such that there was no oversaturation. To ease this, a black screen was placed in front of the flame to block direct light. The negative image of one result is shown in Figure 5.4.

Figure 5.4: The negative of a photo resulting from the angular distribution measurement. Some relatively strong reflection of the mounts is clearly visible. However, this does not interfere with the measurement as they are placed behind the ping pong balls. The difference of reflection between the ping pong balls is also clearly visible.

A mask was created in MATLAB which filters the noise and unwanted data from the image. The result after filtering is shown in Figure 5.5.
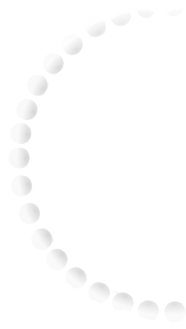
Figure 5.5: The result of the photo of the angular distribution measurement after applying a mask to filter the noise. The reflections of the mounts are filtered as well as any noise in between two neighboring ping pong balls.

By defining the flame location and calculating the angle and intensity of each pixel, a plot in polar coordinates has been made which shows the relative angular intensity of the flame radiation.

The first attempt was performed with the larger samples mounted by wrapping and clamping it in a tungsten wire, but the result was not satisfactory. It is thought that the relatively thick tungsten wire had a major effect on the angular distribution by blocking a part of the radiation.

A second attempt made with small samples of 3 mm long from the 3 mm diameter magnesium wire, mounted on top of a thoriated tungsten wire with a diameter of 100 µm. This clearly provided more consistent results. One of the results is shown in Figure 5.6.
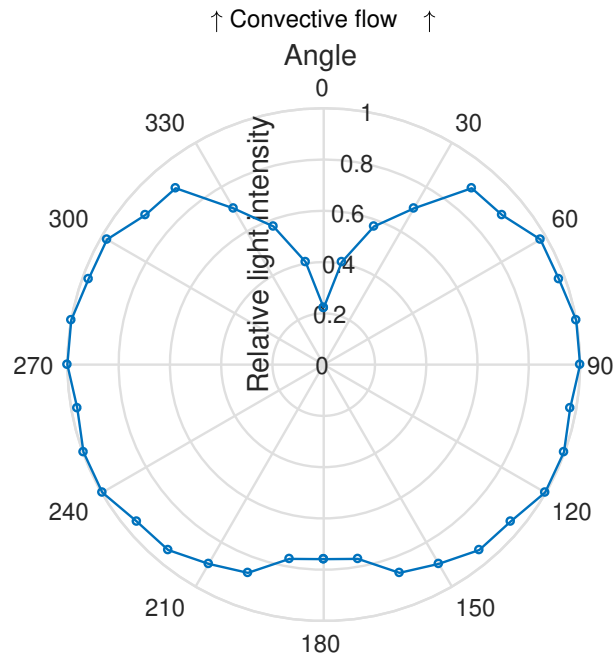
Figure 5.6: Angular distribution of the radiation of the combustion of a magnesium sample. The used sample was a small cylinder of 3 mm cut from a pure magnesium wire with a diameter of 3 mm.

The result is a good resemblance of Figure 4.2. The main difference in Figure 5.6 is the lower intensity beneath the flame. This is believed to be caused by the mount which partly blocks the radiation beneath the flame. The lower intensity at the top of the flame is caused by the smoke which blocks the radiation. At 40° there also appears to be a small peak in intensity. This peak is not visible in Figure 4.2 as the intensity was not measured at that point.

The isotropy factor as calculated by Equation (4.1) is 0.93.

5.2.2 Radiated energy

Multiple magnesium samples of different sizes cut from the ribbon and 2.4 mm wire have been burned and the power of the flame was recorded. The results are plotted in Figure 5.7.
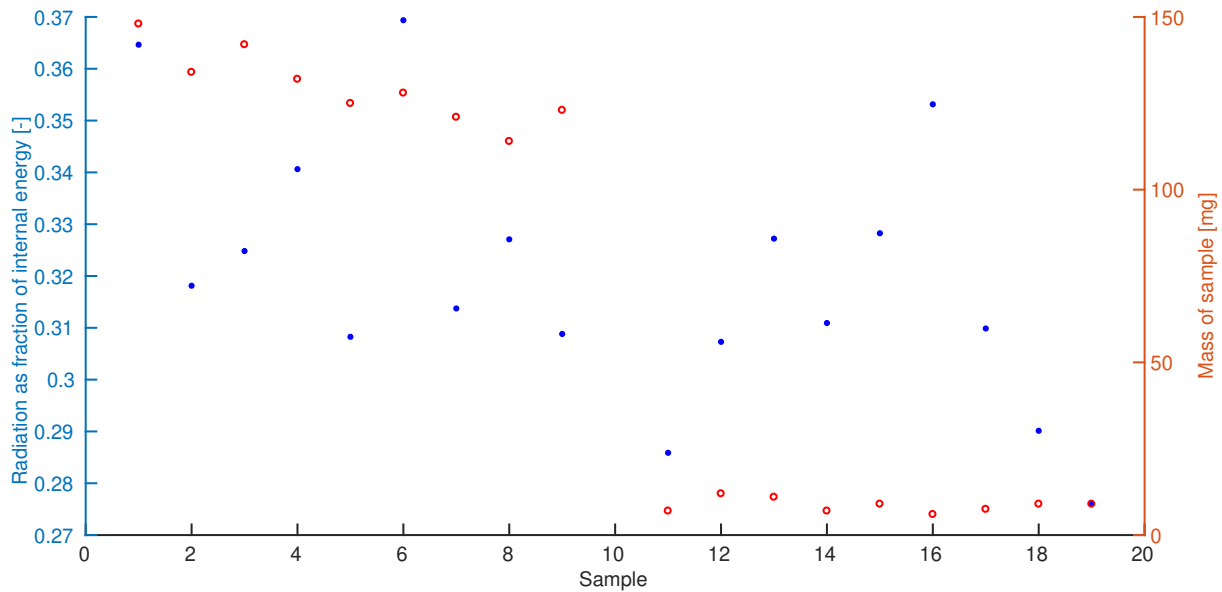
Figure 5.7: Radiated energy of magnesium samples as fraction of the internal energy. The first nine samples were made from 2.4 mm wire and the last nine were made from a magnesium ribbon. The mass of each sample is also shown.

The average fraction of radiated energy is approximately 31 %. This is lower than the 40 % as measured by Shoshin and Altman. The exact cause of this difference is not known and could be attributed to multiple factors. For instance, the particles used in their research were spherical and the samples used in this research either cylindrical or flat. Also, the combustion environment was not controlled in any way. The operating temperature was always room temperature. As the radiated energy for magnesium is mainly attributed to ultra fine oxide particles [11], the amount of smoke generated or the convection around the flame could have a major impact. More detailed research is required to examine these effects.

Another measurement was performed with the pure magnesium wire of 3 mm, from which samples of 3 mm were cut. These small cylindrical samples are a closer approximation of a sphere. This time, a metal plate was placed in front of the laser power meter which was removed upon starting the measurement to act as a shutter. The reason for using this approach is that the laser power meter is also sensitive for (infrared) radiation originating from the person igniting the samples. The result of this measurement is shown in Figure 5.8.
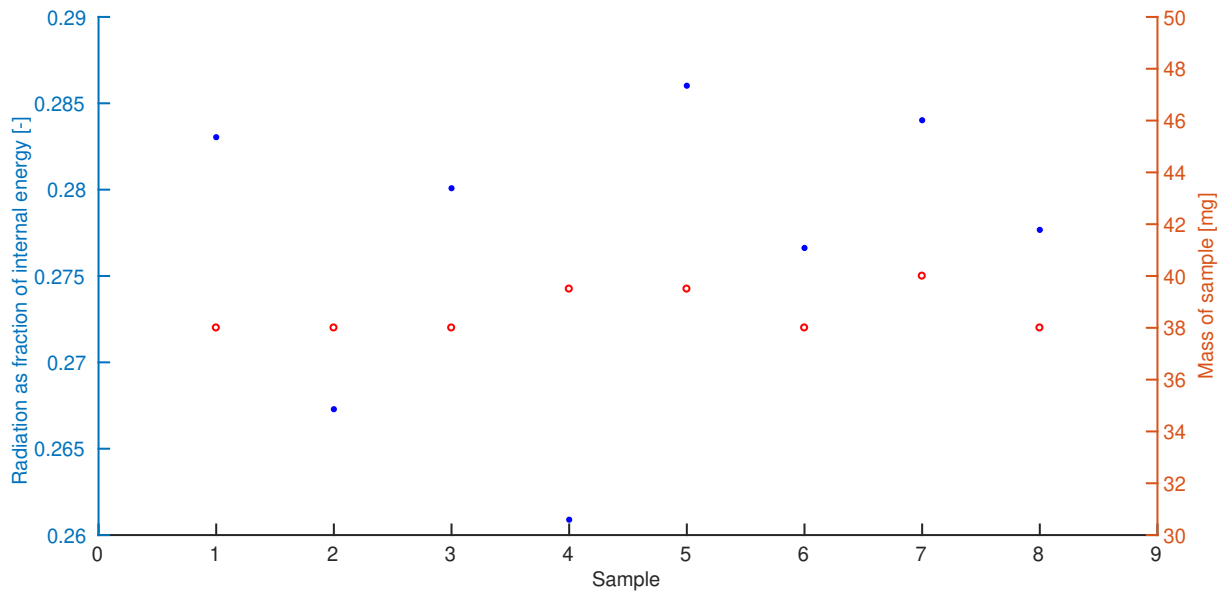
Figure 5.8: Radiated energy of magnesium samples as fraction of the internal energy. All of the samples were hand cut from a 3 mm pure magnesium wire. The mass of each sample is also shown.

The fraction of radiated energy is slightly lower than in the previous measurement, but also more consistent. It was thought that the manual removing of the metal shutter plate caused the slight decrease in radiated energy. However, using a solenoid as electronic shutter did not increase the measured radiated energy.

The lower radiated energy could possibly also be attributed to the smaller and different sample sizes compared to the previous measurement. Again, in-depth research is required to define the exact effects of sample geometry on the amount of radiated energy.

5.2.3 Spectrum

As explained in Section 4.1.3, the spectrum of a magnesium flame has been measured. First, samples of the ribbon and of the wire of 2.4 mm were measured. The relative spectral irradiance measured upon combustion of these samples is shown in Figure 5.9.
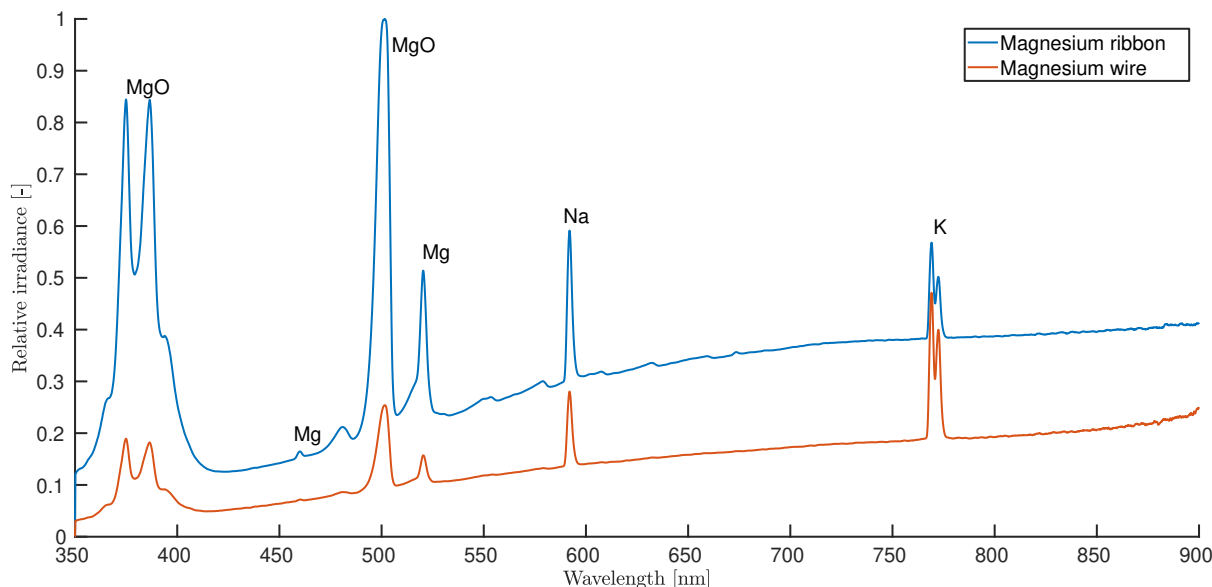
Figure 5.9: Relative irradiance of the combustion of a sample of magnesium wire and ribbon. Both sample were burned in the same setup, in which the cosine corrector was placed approximately 30 cm from the flame. The spectral peaks are indicated.

As can be seen in the figure, the irradiance from the wire sample is much lower. During the experiment this was also clearly noticeable by the burn duration. The ribbon would burn quickly and extremely bright, whereas the wire was significantly less bright and could burn for a duration up to 30 s. This is easily explained by the fact that the surface-to-volume ratio of the ribbon is much higher than that of a wire. The magnesium wire also sometimes showed signs of incomplete combustion. The wire would melt and form a clump of magnesium of which the core would stay intact. This is likely caused by the deposition of the insulative magnesium oxide on the surface.

Another interesting difference between the two samples is the relative difference between the peaks in the spectrum. For the ribbon sample, the largest peak is at ≈750 nm, where as for the wire samples this peak is much lower than the other peaks. Unfortunately the exact composition of the samples is unknown, but the difference could be caused by different levels of impurities in the magnesium. This could also imply that the shape of the spectrum can be altered by choosing the right levels of impurities. For example, to get more infrared or ultraviolet radiation.

Finally, distinct spectral peaks can be seen in the spectrum. These peaks are the result of molecular emission. One would obviously expect spectral peaks from magnesium and its combustion products. Newman and Payne state that the spectrum of Mg has a triplet at 517 nm, and a singlet at 457 nm and 285 nm [37]. These peaks can be seen in the figure. Note that the spectral resolution is too small to resolve the triplet and it shows as a single peak. The peaks at ≈380 nm are attributed to the MgO band, as well as the peaks at 490 nm and 500 nm [38]. There is one small peak left at 480 nm which could not be clearly identified.

Three peaks remain which cannot be attributed to magnesium. The peak at 589 nm is most likely caused by the emission of sodium, whereas the doublet at 766 nm is the result of the emission of potassium [39]. Magnesium samples are not expected to contain sodium or potassium, thus these peaks are most likely caused by a contamination. Another measurement was made where samples of magnesium ribbon were first sanded and cleaned. A measured spectrum is shown in

Figure 5.10.
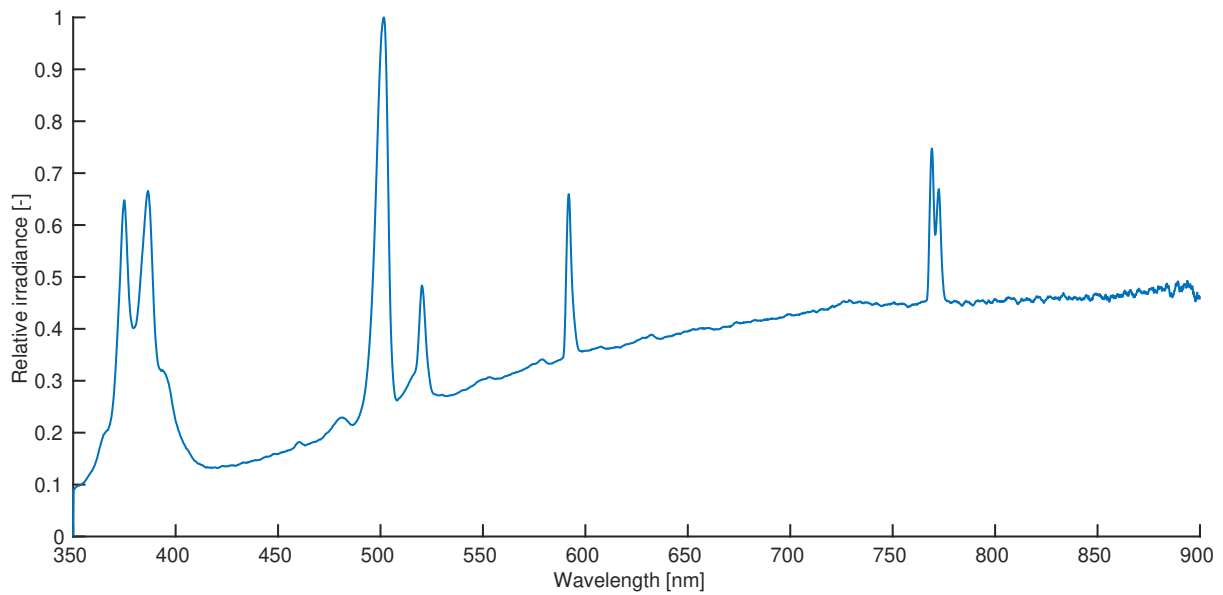
Figure 5.10: Relative irradiance of a sanded and cleaned sample of magnesium ribbon. Any contaminations on the surface of the magnesium samples were removed, but the sodium and potassium peaks did not disappear.

The sodium and potassium peaks are still clearly visible in the figure. As the samples were cleaned, the contamination is probably located in the used equipment. Both elements are present on the skin in the form of a salt. This is likely the origin of the contamination.

Finally, to verify that the spectrum does not depend on the geometry of the sample, samples of different lengths and weights of the 2.4 mm wire have been measured, as shown in Figure 5.11.
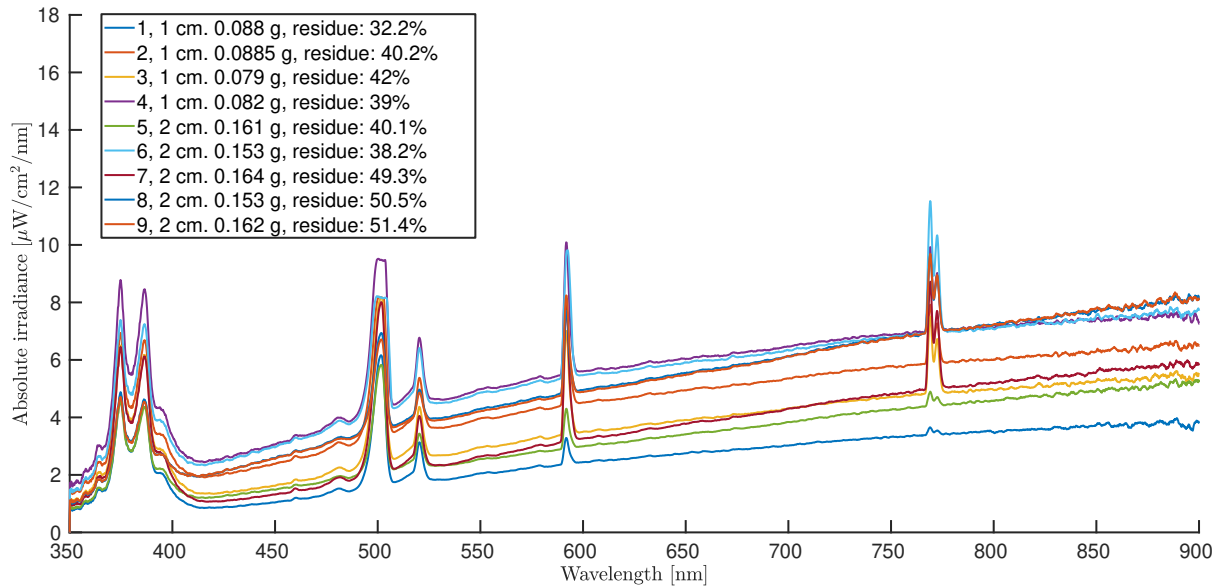
Figure 5.11: Absolute irradiance of samples of different lengths and weights. The absolute irradiance is only an instantaneous measurement during the combustion, and is not measured at the same time for each sample.

The residue of each sample as the ratio of molecular magnesium before and after combustion is also shown in the legend of the plot. The residue for the larger samples appears to be larger than that of the smaller samples. The total amount of residue is much larger than the $(18 \pm 3)\,\%$ as measured by Shoshin and Altman [2]. This could be caused by the larger sample size which leads to a lower surface-to-volume ratio and possibly less burning in the vapor phase. It is clear that the shape of the spectrum barely changes for different samples. The absolute irradiance differs, but this might be due to measuring at a different instant during combustion, or a larger energy release from heavier samples.

The radiated energy measured by the spectrometer was also compared to the radiated energy as measured by the laser power meter. Unfortunately, these results were inconsistent and ranged from $\dfrac{E_{vis}}{E_{rad}} = 0.4$ to 0.8. Even after numerous attempt no consistent results were obtained and it is thought that the spectrometer is not able to consistently measure the radiated energy of variable light sources.

Black body temperature

The black body temperature of the acquired spectra has been calculated with the MATLAB scripts as shown in Appendix F. Figure 5.12 shows one of the acquired spectra and the resulting curve fit.
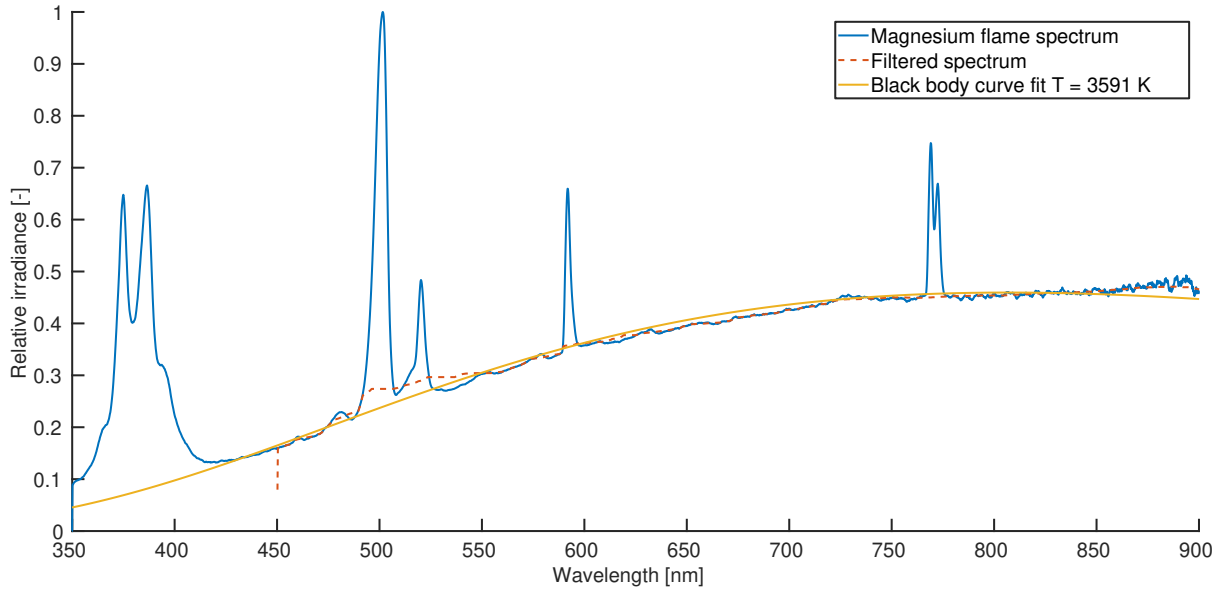
Figure 5.12: Curve fit of a magnesium spectrum with Planck's law. The blue line shows the spectrum as measured by the (calibrated) spectrometer. The red line shows this same spectrum after removing and smoothing the peaks. Finally, the yellow line shows the irradiance calculated with Planck's law which fits the spectrum best.

The figure shows that the peaks below 450 nm have been filtered. Obviously, these peaks are not caused by black body radiation and preserving them would cause a large deviation in the rest of the (fitted) black body spectrum. For this particular measurement, the calculated black body temperature is 3591 K. The deviation between different measurements was approximately 20 K. Note that this temperature should be regarded as the color temperature and does not necessarily provide information about the actual combustion temperature.

The acquired spectrum can be extrapolated into infrared by using the calculated black body temperature and Planck's law. This is shown in Figure 5.13. From here on, when the spectrum of magnesium is mentioned it refers to this measured and extrapolated spectrum. However, the actual infrared spectrum can differ from this extrapolation as magnesium combustion is a multi-temperature system. Thus, the actual infrared spectrum should definitely be measured and verified, but for now it is assumed that it behaves as a black body. This assumption should be kept in mind when new conclusions are drawn from the extrapolated results.
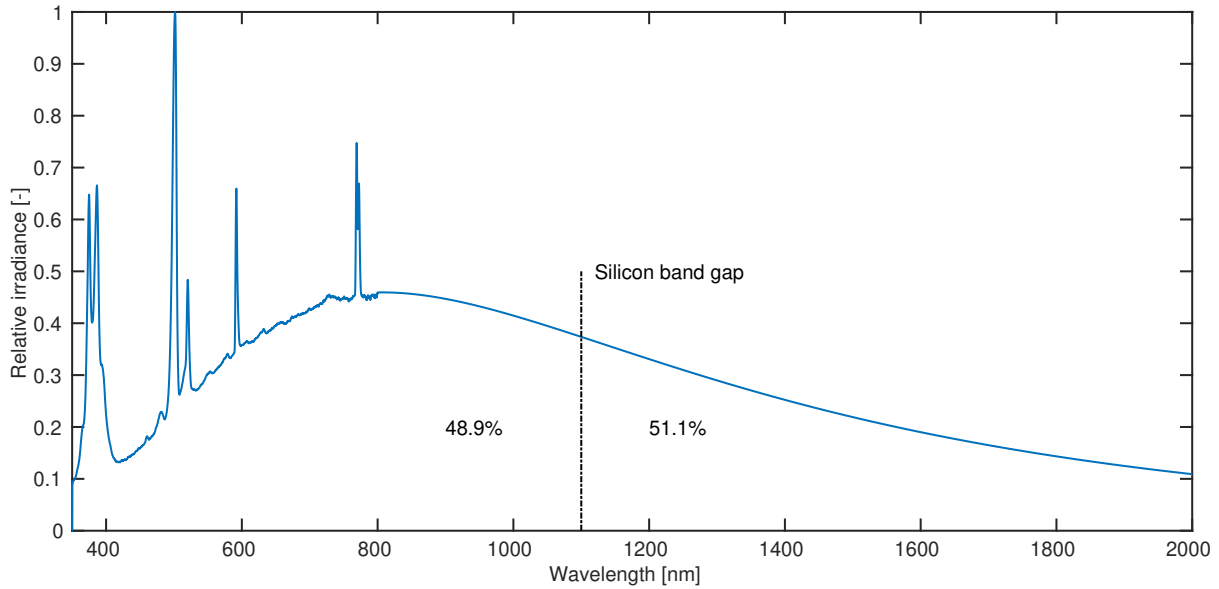
Figure 5.13: Measured and extrapolated spectrum of a magnesium flame. The acquired spectrum from a (calibrated) spectrometer has been extended into the infrared range by applying Planck's law. The percentages show the amount of energy below and above the bandgap of silicon.

The spectrum from 350 nm to 850 nm is provided by the measured spectrum and the irradiance in the infrared region is provided by extrapolating the data with Planck's law. The wavelength as defined by the bandgap of silicon is also shown in the figure. The percentage of energy above the bandgap of silicon, thus the energy which can be captured with a silicon photovoltaic cell, is 48.9%. The energy in the infrared region is 51.1%. This means that slightly more than half of the energy in the magnesium spectrum cannot be absorbed by a silicon photovoltaic cell.

5.3 Photovoltaic energy harvesting

5.3.1 Spectral mismatch

Based on the theoretically extended spectrum from the previous section, the difference between the energy in the spectrum and the absorbed energy by the semiconductor can be estimated. Figure 5.14 has been created using the MATLAB function as provided in Appendix G.
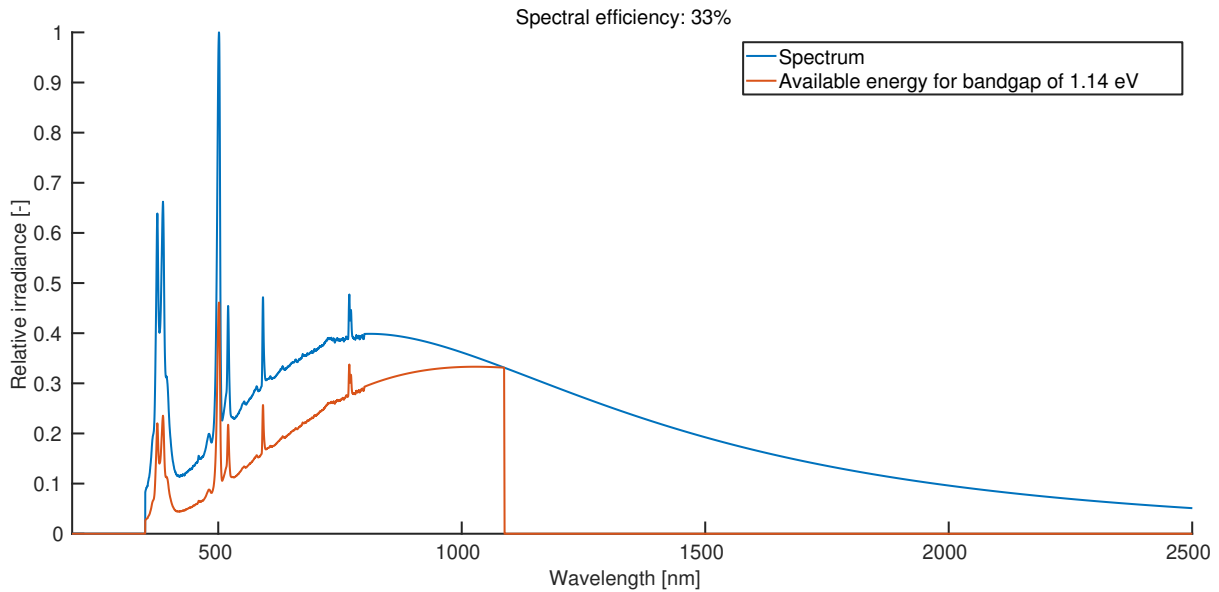
Figure 5.14: Spectral mismatch between the theoretically extended magnesium spectrum and a silicon solar cell. In contrast to the solar spectrum, a substantial part of the radiation is located in the infrared range. In addition, the large molecular emission peaks are poorly absorbed. The spectral mismatch leads to a maximum efficiency of 33% for a silicon photovoltaic cell.

It can be seen that the spectrum of magnesium is hard to match with a single semiconductor. The molecular emission peaks require a high bandgap whereas the infrared gray body radiation requires a low bandgap. For a silicon photovoltaic cell with a bandgap of $1.14\,\text{eV}$, the maximum achievable efficiency based on the spectral mismatch is 33.0% (whereas for the solar spectrum it is 48.8%).

As explained in Section 3.3, different semiconducting materials can be used for a solar cell. As there is a larger fraction of energy contained in the infrared range as compared to the solar spectrum, a semiconducting material with a lower bandgap is probably preferable. The bandgap for the highest possible efficiency was calculated by iterating over a range of bandgaps. The resulting optimal bandgap appears to be $0.68\,\text{eV}$. The spectral mismatch for this bandgap is shown in Figure 5.15.
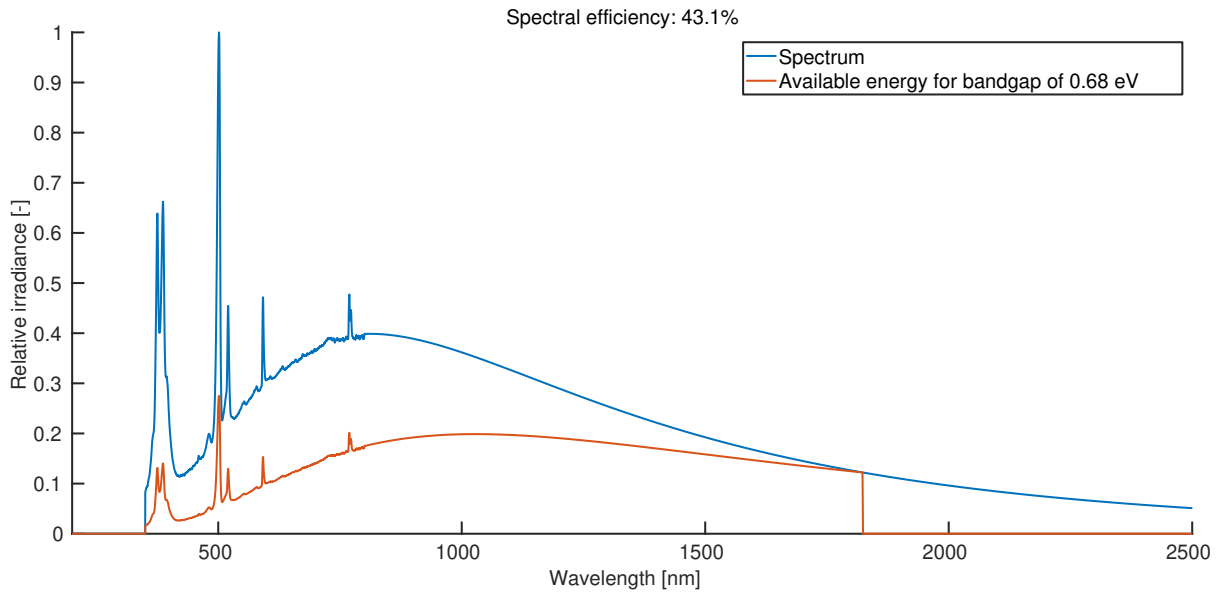
Figure 5.15: Spectral mismatch between the theoretically extended magnesium spectrum and a photovoltaic cell with a bandgap of 0.68 eV. The lower bandgap compared to silicon results in a higher spectral efficiency of 43.1%.

As expected, a photovoltaic cell with a lower bandgap will achieve a higher spectral efficiency for the theoretically extended magnesium spectrum. The calculation can also be applied to find the optimal bandgaps for a multi-junction cell. This is shown in Figure 5.16.
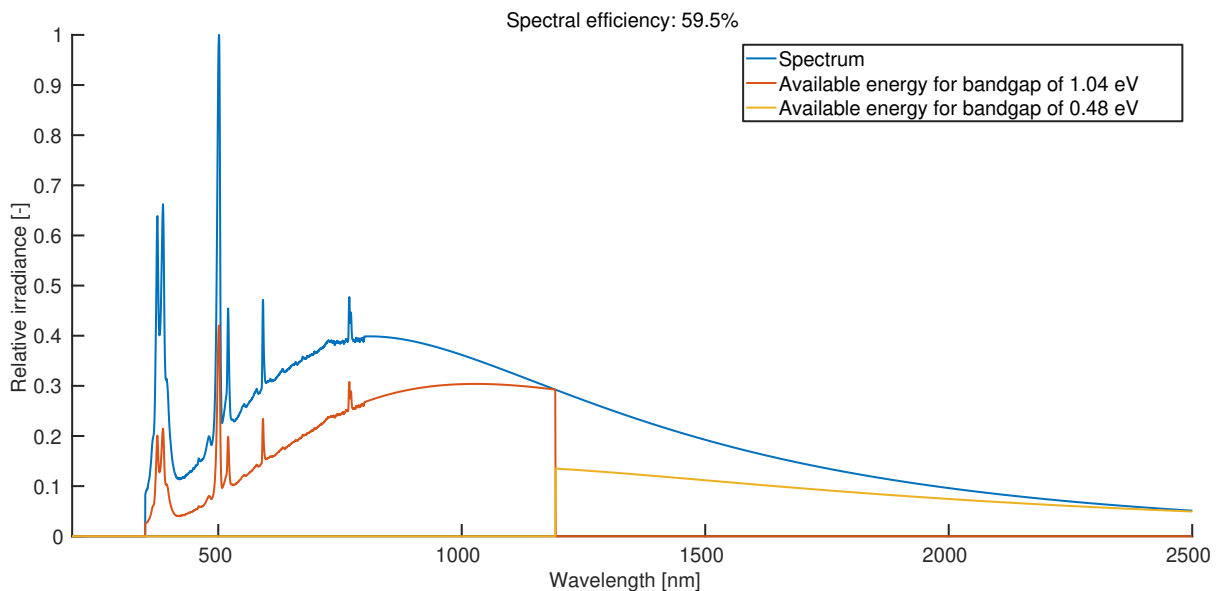
Figure 5.16: Spectral mismatch between the theoretically extended magnesium spectrum and a dual-junction photovoltaic cell. The optimal bandgaps are 1.04 eV and 0.48 eV

The resulting spectral efficiency for a dual-junction photovoltaic cell is greatly increased to 59.5%. Please note that these are all theoretical results. The real spectrum of a magnesium flame will need to be measured. Also, the semiconducting materials for the optimal bandgaps might not

exist or might have a poor conversion efficiency.

6 Discussion

In the previous chapter, the results of the experiments have been shown and analyzed. Some of the results were as expected, others differed from the initial expectations. In this chapter the results will be discussed.

By combining the individual results of the previous chapter, an estimation of the overall efficiency of a photovoltaic energy harvesting system for metal flames can be made. Based on this estimation, propositions are made to increase the efficiency.

6.1 Radiated energy

The results have shown that the measured radiated energy of magnesium samples (28 % to 31 %) is noticeably lower than expected (40 %). The exact cause of this difference is not known. The measurements performed by Shoshin and Altman used a different setup as has been used in this research. They have used a calorimeter which had been calibrated at temperatures of 1100 K, 1200 K and 1300 K. The laser power meter used in this research has a flat thermal absorption up until the far infrared range. Comparison with the calibrated spectrometer has shown that the measured power is correct in at least the visible range. However, the aligning of equipment and the actual measurement have all been performed manually. This may or may not have an effect on the results, but for future measurements it is advised to automate tasks such as ignition of the sample and opening of the shutter. Also, the measurement should be ideally performed in a carefully aligned setup which is placed in total darkness.

As the exact combustion mechanism of magnesium is not clearly identified, the sample geometry or combustion environment might also affect the amount of radiation. For the purpose of photovoltaic energy harvesting, one could simply try different samples or setups. In the ideal case however, the exact combustion mechanism of metals should be researched.

6.2 Spectrum

The sample geometry does not seem to affect the (relative) spectrum of the magnesium flames. Because of the available equipment, only the spectrum in the visible range could be measured. The spectrum into the infrared range has been extrapolated using Planck's law. In order to verify this extrapolation, the actual spectrum in the infrared range should be measured. This could also be performed by measuring $\dfrac{E_{vis}}{E_{rad}}$ and comparing it to the theoretical result. An attempt was made to measure this value, but the results were inconsistent. It might be that the spectrometer is unable to measure the absolute irradiance of variable light sources correctly.

The sodium and potassium contaminations in the setup are clearly visible in the results. These contaminations are unwanted for defining the actual spectrum of a magnesium flame, but for harvesting the radiative energy with a photovoltaic cell they might be useful. As shown in Section 5.3.1, there is a large spectral mismatch between the magnesium and magnesium oxide spectral peaks for a silicon solar cell. For the sodium and potassium peaks this spectral mismatch is significantly smaller, however the intensity of these peaks is also weak. Possibly, the spectral mismatch of a metal flame could be reduced by coloring the flame with the use of additives, such as NaK salt for example.

6.3 Efficiency

By multiplying the fraction of energy lost by radiation with the spectral mismatch of the photovoltaic cell, the maximum (spectral) efficiency of the system can be calculated. In the ideal case (the larger samples with a multi-junction photovoltaic cell) this would be $31\% \cdot 59.5\% = 18.4\%$. For a silicon photovoltaic cell it would be $31\% \cdot 33\ = 10.2\%$. If we assume that modern photovoltaic cells have an efficiency approximately half of the maximum attainable spectral efficiency, and that all emitted radiation is captured, this would result in an efficiency of 5.1%. This value appears to be rather low, but it depends on the perspective. One of the first experimental research projects on thermophotovoltaics reached a record efficiency of 3.2% [40]. More recent research has shown that thermophotovoltaic systems are capable of achieving effciencies from 10% [41] up to 24.1% [42]. These however used specific emitters and photovoltaic cells to reach those efficiencies. Thermophotovoltaics is a relatively new field of research and I believe that the efficiency of such systems will be greatly increased in the future. I also believe that solar photovoltaics will be the main energy source in the future and that photovoltaic technology will be greatly improved the coming decade.

A major benefit of a thermophotovoltaic system is that is contains no moving parts and does not require any specific conditions. As long as the spectrum is matched by the photovoltaic cell, and the temperature of the cell is kept between the operating limits, it will work. In the case of unlikely misuse, the components can be easily and cheaply replaced. This, in particular, is true when a metal flame is used instead of an emitter.

6.4 Magnesium combustion

All measurements have been performed with non-controlled magnesium-air flames. One of the main problems with the high flame temperature of magnesium is the large NOx production. This could probably be prevented by using a stoichiometric ratio of magnesium and oxygen in the mixture, as there will be no oxygen left to react with nitrogen. A different method could be by burning magnesium with a different reactant such as pure carbon dioxide, which contains no nitrogen. This would prevent NOx production and will produce carbon and thus the reaction will be carbon negative. A different method would be to reduce the flame temperature. This will reduce the radiative power of the flame, but if one could limit the convective heat loss, the amount of radiated energy will not change. The radiation will be shifted towards infrared however, which means that photovoltaic cells with a lower bandgap are required in that case. The feasibility of these approaches and the corresponding radiative energy which is released should be researched.

The next step should be to first analyze the radiative energy release of a magnesium powder flame. For practical purposes, the results of a powder flame will be more useful than those of solid magnesium samples. A proper metal fuel burner should be able to start and stop on command and function continuously for long periods. Both of these are not possible, or very difficult, with solid magnesium samples.

6.5 Thermophotovoltaics

This research project focused on converting direct radiation of a metal flame into electricity. This is similar to what is normally performed with thermophotovoltaics, but there is an important difference. The leftover heat after capturing the radiation is still wasted when only direct radiation is used. By using the leftover heat for conventional thermophotovoltaics, the efficiency of the system can be increased. At the time of writing, the efficiency of thermophotovoltaic systems

is still quite poor. However, the theoretical efficiency is only limited by the Carnot efficiency and major improvements of such systems have already been made in a short period of time. For that reason, I expect that in the future thermophotovoltaic systems will be able to compete with for example internal combustion engines.

7 Conclusion

For small cylindrical magnesium samples of $3\,\mathrm{mm} \times 3\,\mathrm{mm}$ it was found that the radiative energy loss is approximately $28\,\%$ of the total heat release. For larger samples this value was slightly higher at approximately $31\,\%$.

The maximum spectral efficiency for a silicon photovoltaic cell for the spectrum of magnesium is estimated to be $33\,\%$. This is significantly lower than the maximum efficiency which such a cell can achieve with the solar spectrum. However, by choosing a semiconducting material with a lower bandgap, or by using a multi-junction photovoltaic cell, the spectral efficiency can be greatly increased.

This spectral efficiency was estimated by extrapolating the visible spectrum into the infrared range with Planck's law. This assumption will have to be verified, as a magnesium flame is not a single temperature system. An infrared spectrometer can be used for this verification.

An overall efficiency of 5% should be achievable with a silicon photovoltaic system which captures all of the radiation emitted by a magnesium flame. The fact that such a system contains no moving parts and is relatively cheap are two major benefits. Also, the efficiency can likely be greatly increased by controlling the combustion parameters and choosing the appropriate photovoltaic cells. For these reasons, a photovoltaic system is considered to be a feasible low-efficiency option at this moment. It is recommended to conduct more research in order to improve the efficiency in the future.

Bibliography

[1] J. Bergthorson, S. Goroshin, M. Soo, P. Julien, J. Palecka, D. Frost, and D. Jarvis, "Direct combustion of recyclable metal fuels for zero-carbon heat and power," *Applied Energy*, vol. 160, pp. 368 –382, 2015, ISSN: 0306-2619. DOI: http://doi.org/10.1016/j.apenergy.2015.09.037. [Online]. Available: http://www.sciencedirect.com/science/article/pii/S0306261915011071.

[2] Y. L. Shoshin and I. S. Altman, "Integral radiation energy loss during single mg particle combustion," *Combustion Science and Technology*, vol. 174, no. 8, pp. 209–219, 2002. DOI: 10.1080/00102200290021326. eprint: http://dx.doi.org/10.1080/00102200290021326. [Online]. Available: http://dx.doi.org/10.1080/00102200290021326.

[3] U. Bossel, "Does a hydrogen economy make sense?" *Proceedings of the IEEE*, vol. 94, no. 10, pp. 1826–1837, 2006, ISSN: 0018-9219.

[4] P. Boris, "A study of the flammability of magnesium," Federal Aviation Agency, Tech. Rep., 1964.

[5] E. L. Dreizin, C. H. Berman, and E. P. Vicenzi, "Condensed-phase modifications in magnesium particle combustion in air," *Combustion and Flame*, vol. 122, no. 1–2, pp. 30 –42, 2000, ISSN: 0010-2180. DOI: https://doi.org/10.1016/S0010-2180(00)00101-2. [Online]. Available: http://www.sciencedirect.com/science/article/pii/S0010218000001012.

[6] E. L. Dreizin and V. K. Hoffmann, "Experiments on magnesium aerosol combustion in microgravity," *Combustion and Flame*, vol. 122, no. 1–2, pp. 20 –29, 2000, ISSN: 0010-2180. DOI: https://doi.org/10.1016/S0010-2180(00)00099-7. [Online]. Available: http://www.sciencedirect.com/science/article/pii/S0010218000000997.

[7] H. Cassel and I. Liebman, "Combustion of magnesium particles i," *Combustion and Flame*, vol. 6, pp. 153 –156, 1962, ISSN: 0010-2180. DOI: http://dx.doi.org/10.1016/0010-2180(62)90084-6. [Online]. Available: http://www.sciencedirect.com/science/article/pii/0010218062900846.

[8] J. Lim, Guidance, Navigation, and Control and Co-located Conferences, 2010, 0. DOI: 10.2514/6.2010-6676. [Online]. Available: http://dx.doi.org/10.2514/6.2010-6676.

[9] H. Cassel and I. Liebman, "Combustion of magnesium particles ii - ignition temperatures and thermal conductivities of ambient atmospheres," *Combustion and Flame*, vol. 7, pp. 79 –81, 1963, ISSN: 0010-2180. DOI: http://dx.doi.org/10.1016/0010-2180(63)90157-3. [Online]. Available: http://www.sciencedirect.com/science/article/pii/0010218063901573.

[10] P. Garra, G. Leyssens, O. Allgaier, C. Schönnenbeck, V. Tschamber, J.-F. Brilhac, T. Tahtouh, O. Guézet, and S. Allano, "Magnesium/air combustion at pilot scale and subsequent {pm} and {nox} emissions," *Applied Energy*, vol. 189, pp. 578 –587, 2017, ISSN: 0306-2619. DOI: https://doi.org/10.1016/j.apenergy.2016.12.069. [Online]. Available: http://www.sciencedirect.com/science/article/pii/S0306261916318347.

[11] Y. L. Shoshin and I. S. Altman, "Quantitative measurement of flame generated particulate oxide by interferometry technique," *International Journal of Energetic Materials and Chemical Propulsion*, vol. 5, no. 1-6, pp. 773–780, 2002, ISSN: 2150-766X.

[12] F. Erogbogbo, T. Lin, P. M. Tucciarone, K. M. LaJoie, L. Lai, G. D. Patki, P. N. Prasad, and M. T. Swihart, "On-demand hydrogen generation using nanosilicon: Splitting water without light, heat, or electricity," *Nano Letters*, vol. 13, no. 2, pp. 451–456, 2013, PMID: 23317111. DOI: 10.1021/nl304680w. eprint: http://dx.doi.org/10.1021/nl304680w. [Online]. Available: http://dx.doi.org/10.1021/nl304680w.

[13] P. Chakraborty and M. R. Zachariah, "Do nanoenergetic particles remain nano-sized during combustion?" *Combustion and Flame*, vol. 161, no. 5, pp. 1408 –1416, 2014, ISSN: 0010-2180. DOI: http://dx.doi.org/10.1016/j.combustflame.2013.10.017. [Online]. Available: http://www.sciencedirect.com/science/article/pii/S001021801300391X.

[14] B. Piriou, G. Vaitilingom, B. Veyssière, B. Cuq, and X. Rouau, "Potential direct use of solid biomass in internal combustion engines," *Progress in Energy and Combustion Science*, vol. 39, no. 1, pp. 169 –188, 2013, ISSN: 0360-1285. DOI: https://doi.org/10.1016/j.pecs.2012.08.001. [Online]. Available: http://www.sciencedirect.com/science/article/pii/S0360128512000536.

[15] A. Demirbas and F. Meydan, "Utilization of biomass as alternative fuel for external combustion engines," *Energy Sources*, vol. 26, no. 13, pp. 1219–1226, 2004. DOI: 10.1080/00908310390268065. eprint: http://dx.doi.org/10.1080/00908310390268065. [Online]. Available: http://dx.doi.org/10.1080/00908310390268065.

[16] N. P. Nightingale, "Automotive stirling engine: Mod 2 design report," Mechanical Technology, Inc., Latham, NY, United States; NASA, Tech. Rep., 1986.

[17] K. Al-attab and Z. Zainal, "Externally fired gas turbine technology: A review," *Applied Energy*, vol. 138, pp. 474 –487, 2015, ISSN: 0306-2619. DOI: http://dx.doi.org/10.1016/j.apenergy.2014.10.049. [Online]. Available: http://www.sciencedirect.com/science/article/pii/S030626191401099X.

[18] M. Kautz and U. Hansen, "The externally-fired gas-turbine (efgt-cycle) for decentralized use of biomass," *Applied Energy*, vol. 84, no. 7-8, pp. 795–805, 2007, Industrial Energy Analysis and Management: A European Perspective, ISSN: 0306-2619. DOI: http://dx.doi.org/10.1016/j.apenergy.2007.01.010. [Online]. Available: http://www.sciencedirect.com/science/article/pii/S030626190700013X.

[19] S. B. Ferreira and P. Pilidis, "Comparison of externally fired and internal combustion gas turbines using biomass fuel," *Journal of Energy Resources Technology*, vol. 123, no. 4, pp. 291–296, 2001, ISSN: 0195-0738. DOI: 10.1115/1.1413468. [Online]. Available: http://dx.doi.org/10.1115/1.1413468.

[20] *Ultra micro gas turbine generator*, http://www.powermems.be/gasturbine.html, Accessed: 2016-02-22.

[21] A. H. Epstein, S. A. Jacobson, J. M. Protz, and L. G. Frechette, "Shirtbutton-sized gas turbines: The engineering challenges of micro high speed rotating machinery," *Proceedings of the 8th International Symposium on Transport Phenomena and Dynamics of Rotating Machinery*, 2000.

[22] J. Peirs, D. Reynaerts, and F. Verplaetsen, "A microturbine for electric power generation," *Sensors and Actuators A: Physical*, vol. 113, no. 1, pp. 86 –93, 2004, ISSN: 0924-4247. DOI: http://dx.doi.org/10.1016/j.sna.2004.01.003. [Online]. Available: http://www.sciencedirect.com/science/article/pii/S0924424704000081.

[23] T. Bauer, *Thermophotovoltaics: Basic Principles and Critical Aspects of System Design*, ser. Green Energy and Technology. Springer Berlin Heidelberg, 2011, ISBN: 9783642199653. [Online]. Available: https://books.google.nl/books?id=f62s3FILc4UC.

[24] *Pn junction theory*, http://www.electronics-tutorials.ws/diode/diode_2.html, Accessed: 11-4-2017.

[25] *Lecture notes of 4se00 - sustainable energy sources*, 2015.

[26] W. Shockley and H. J. Queisser, "Detailed balance limit of efficiency of p-n junction solar cells," *Journal of Applied Physics*, vol. 32, no. 3, pp. 510–519, 1961. DOI: `10.1063/1.1736034`. eprint: `http://dx.doi.org/10.1063/1.1736034`. [Online]. Available: `http://dx.doi.org/10.1063/1.1736034`.

[27] S. Rühle, "Tabulated values of the shockley–queisser limit for single junction solar cells," *Solar Energy*, vol. 130, pp. 139 –147, 2016, ISSN: 0038-092X. DOI: `https://doi.org/10.1016/j.solener.2016.02.015`. [Online]. Available: `http://www.sciencedirect.com/science/article/pii/S0038092X16001110`.

[28] I. Etxebarria, A. Furlan, J. Ajuria, F. W. Fecher, M. Voigt, C. J. Brabec, M. M. Wienk, L. Slooff, S. Veenstra, J. Gilot, and R. Pacios, "Series vs parallel connected organic tandem solar cells: Cell performance and impact on the design and operation of functional modules," *Solar Energy Materials and Solar Cells*, vol. 130, pp. 495 –504, 2014, ISSN: 0927-0248. DOI: `https://doi.org/10.1016/j.solmat.2014.07.047`. [Online]. Available: `http://www.sciencedirect.com/science/article/pii/S0927024814004164`.

[29] D. P. Hohm and M. E. Ropp, "Comparative study of maximum power point tracking algorithms," *Progress in Photovoltaics: Research and Applications*, vol. 11, no. 1, pp. 47–62, 2003, ISSN: 1099-159X. DOI: `10.1002/pip.459`. [Online]. Available: `http://dx.doi.org/10.1002/pip.459`.

[30] D. J. Williams and L. M. Fraas, "Demonstration of a candle powered radio using gasb thermophotovoltaic cells," *AIP Conference Proceedings*, vol. 358, no. 1, pp. 134–137, 1996. DOI: `10.1063/1.49682`. eprint: `http://aip.scitation.org/doi/pdf/10.1063/1.49682`. [Online]. Available: `http://aip.scitation.org/doi/abs/10.1063/1.49682`.

[31] F. Bouzid and L. Dehimi, "Performance evaluation of a gasb thermophotovoltaic converter," *Revue des Energies Renouvelables*, vol. 15, no. 3, pp. 383 –397, 2012. [Online]. Available: `http://www.cder.dz/download/Art15-3_3.pdf`.

[32] *Magnesium oxide*, `https://webbook.nist.gov/cgi/cbook.cgi?ID=C1309484&Mask=2`, Accessed: 2-5-2018.

[33] *Cree xlamp xm-l data sheet*, `http://www.cree.com/led-components/media/documents/XLampXML.pdf`, Accessed: 30-10-2017.

[34] *S302c - thermal power sensor, stabilized, 0.19 - 25 μm, 2 w*, `https://www.thorlabs.com/thorproduct.cfm?partnumber=S302C`, Accessed: 24-10-2017.

[35] *Hl-3p-cal family*, `https://oceanoptics.com/product/hl-3-cal-hl-3plus-cal-family/`, Accessed: 24-10-2017.

[36] J. Hoek, "The shining power of metal flames," 2018.

[37] R. Newman and J. Payne, "The anomalous brightness of magnesium-air flames," *Combustion and Flame*, vol. 68, no. 1, pp. 31 –41, 1987, ISSN: 0010-2180. DOI: `https://doi.org/10.1016/0010-2180(87)90063-0`. [Online]. Available: `http://www.sciencedirect.com/science/article/pii/0010218087900630`.

[38] E.-C. Koch, V. Weiser, E. Roth, and D. Müller, "Uv-vis spectroscopic investigation of magnesium/fluorocarbon pyrolants," in *Conference paper*, Jul. 2006.

[39] R. W. B. Pearse and A. G. Gaydon, *The Identification of Molecular Spectra*. Chapman Hall Ltd., 1951.

[40] A. Lenert, D. Bierman, Y. Nam, W. R Chan, I. Celanovic, M. Soljačić, and E. N Wang, "Addendum: A nanophotonic solar thermophotovoltaic device," vol. 10, Jan. 2014.

[41] Q. Lu, X. Zhou, A. Krysa, A. Marshall, P. Carrington, C.-H. Tan, and A. Krier, "Inas thermophotovoltaic cells with high quantum efficiency for waste heat recovery applications below 1000°c," *Solar Energy Materials and Solar Cells*, vol. 179, pp. 334 –338, 2018, ISSN: 0927-0248. DOI: https://doi.org/10.1016/j.solmat.2017.12.031. [Online]. Available: http://www.sciencedirect.com/science/article/pii/S0927024817306773.

[42] D. N. Woolf, E. A. Kadlec, D. Bethke, A. D. Grine, J. J. Nogan, J. G. Cederberg, D. B. Burckel, T. S. Luk, E. A. Shaner, and J. M. Hensley, "High-efficiency thermophotovoltaic energy conversion enabled by a metamaterial selective emitter," *Optica*, vol. 5, no. 2, pp. 213–218, 2018. DOI: 10.1364/OPTICA.5.000213. [Online]. Available: http://www.osapublishing.org/optica/abstract.cfm?URI=optica-5-2-213.

[43] *Operation manual thorlabs instrumentation optical power and energy meter pm100d*, 2011.

[44] *Absolute irradiance calibration & measurement*, http://oceanoptics.com/wp-content/uploads/Absolute-Irradiance-Calibration-Measurement.pdf, Accessed: 12-3-2018.

Appendices

A Angular distribution of flame radiation

The angular distribution of the flame radiation is calculated from a photograph taken of the setup as described in Section 4.1.1. The photo is imported in MATLAB using the Image Processing Toolbox. The input parameters are the location of the flame in the photo, and $d\theta$ for the plot of the angular distribution.

The script first applies a predefined mask to the image to filter everything from the image except for the ping pong balls. The resulting image is rotated such that the top of the flame is at zero degrees in polar coordinates. Finally for every color available, the angle and intensity of every remaining pixel is calculated. The pixel with the maximum intensity within a range of $d\theta$ is plotted in a polar coordinate plot.

The overlayImage() function is a modified version of the imoverlay() function of MATLAB which is able to work with 16 bit images instead of the default 8 bit.

The MATLAB script is shown below.

```matlab
1  clear all; close all;
2
3  xflame = 1520;
4  yflame = 2010;
5  dtheta = deg2rad(10);
6
7  %% Select and load image
8  [file, path] = uigetfile('.tif');
9  [img map] = imread(fullfile(path, file));
10 figure;
11 img = imgaussfilt(img, 2);
12 imshow(img);
13
14 %% Load predefined freehand mask
15 load('mask.mat');
16
17 %% Create masked image
18 % Rotate such that 0 degrees in polar coordinatesis is the top of the flame
19 imgmasked = overlayImage(img,~mask, [0 0 0]);
20 imgmasked = fliplr(rot90((imgmasked)));
21
22 imshow(imgmasked);
23 set(gca,'YDir','normal');
24
25 %% Plot flame location
26 viscircles([xflame yflame], 50)
27
28 figure
29 for (j = 1:size(img, 3))
30     clear A Amax B Bmax
31     I = imgmasked(:, :, j);
32
33     % Skip values of zero
34     minBrightness = 1;
35     [rows cols] = find(I > minBrightness);
36     [ymax xmax] = size(img);
37
38     %% Calculate the angle with respect to the flame for every pixel
39     for i = 1:length(rows)
40         x = cols(i);
41         y = rows(i);
42         [ang rho] = cart2pol(x-xflame, y-yflame);
43         A(i) = ang;
44         B(i) = I(y,x);
45     end
46
47     %% Calculate the maximum value for each angle
```

```matlab
48          Amax = [];
49          Bmax = [];
50
51          % Find maximum intensity from 0 to 180 degrees with defined steps
52          for i = 0:dtheta:max(A)
53              Amax = [Amax i];
54              maxB = double(max(B(find(A > (i-dtheta) & A > 0 & A < max(A) & A < (i+dtheta)))))
                   ;
55              if (isempty(maxB))
56                  maxB = nan;
57              end
58              Bmax = [Bmax maxB];
59          end
60          polarplot([Amax -fliplr(Amax)], [Bmax fliplr(Bmax)]./max(Bmax), 'o-');
61          hold all
62      end
63
64  %% Isotropy
65  Bhor = Bmax(find(Amax == pi/2));
66  N = numel(Bmax);
67  I_i = [];
68  phi_i = [];
69  for j = 1:N-1
70      I_i(j) = (Bmax(j) + Bmax(j+1))/2;
71      phi_i(j) = (Amax(j) + Amax(j+1))/2;
72  end
73  k = sum(I_i .* sin(phi_i)) / (Bhor * sum(sin(phi_i)))
74
75  ax = gca;
76  ax.ThetaZeroLocation = 'top';
77  ax.ThetaDir = 'clockwise';
78  rlim([0 1])
79  ax.ThetaAxis.Label.String = 'Angle';
80  ax.RAxis.Label.String = 'Relative light intensity';
81  title('\uparrow Convective flow \uparrow')
```

B Laser power meter energy measurement

To verify that the laser power meter can be used to measure energy, the setup described in Section 4.1.2 has been used. The results are shown below.

The pulse times that have been measured were in the range of 1 s to 10 s. For each measurement, the energy has been calculated by integrating the power signal, and the pulse time is defined by the photodiode signal. The average laser energy has been calculated by averaging the laser power of all measurements. The results are shown in Figure B.1
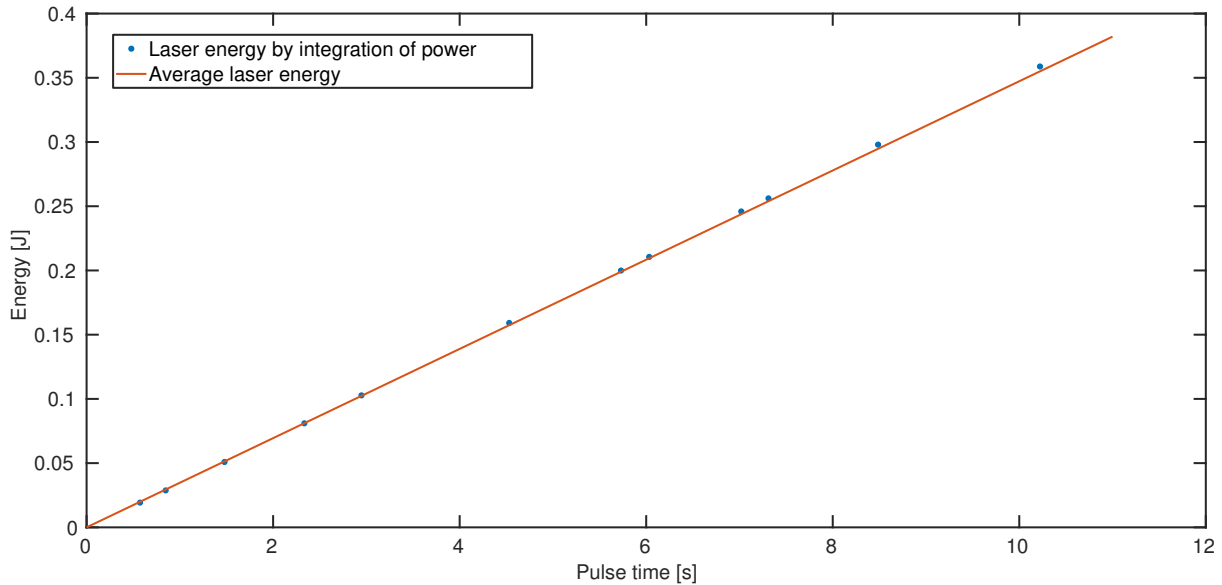

Figure B.1: Laser pulse energy plotted against the pulse time duration. The plot shows that the energy can be calculated by integrating the power signal, irrespective of the pulse time.

The plot shows that all measurements are on the line $E = P \cdot t$. For short pulse times, the calculated energy is slightly below the average laser energy, whereas for longer pulse times it is slightly above the average laser energy. This shift is believed to be caused by faulty zeroing of the sensor. The cold sensor had been zeroed, i.e. no experiments had been performed yet. However, for longer measurements the sensor has to be zeroed in a state of thermal stability [43]. The value of zero will differ when the heat sink of the thermal disk has been heated. Because no thermal stability is reached during the experiment, the actual zero offset will change between short and long pulse time which explains the slight shift in laser energy.

C Precision aperture

For accurate measurements with the laser power meter, it is required that the illuminated area is precisely known. To achieve this, a high precision aperture is used to limit the optical beam diameter. This appendix describes the design of this precision aperture.

As the absolute irradiance is a function of the area, the precision of the measurements is also subjected to the precision of the illuminated area. In contrast to the coherent beam of a laser, the light of a point source is distributed evenly. The aperture is used to limit the absorbed radiation through a precise, fixed area. To avoid problems with vignetting, the inner edge of the aperture is kept as thin as possible.

The aperture is made of copper because of its large thermal conductivity. The large thermal conductivity combined with a relatively large mass prevents local heating of the object which could cause small deformations in the aperture area.

The design of the aperture is shown in Figure C.1.
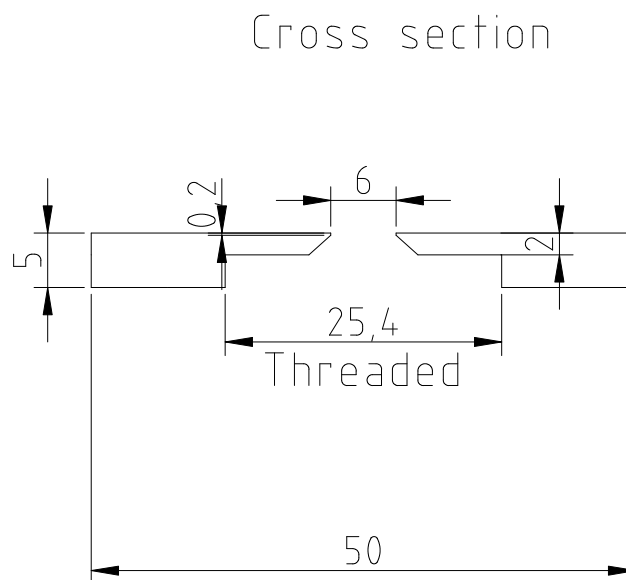
Figure C.1: Design of the precision aperture. The aperture is supposed to be screwed on the SM1 thread that comes along with the laser power meter.

The figure shows that the inner edge of the aperture is kept as thin as possible (0.2 mm). The inner diameter is 6 ± 0.01 mm. The aperture has been manufactured by the Equipment & Prototype Center (EPC) in Eindhoven. A photograph of the aperture as mounted on the laser power meter is shown in Figure C.2

Figure C.2: Photograph of the aperture as mounted on the laser power meter.

D Acquiring spectra in MATLAB

The Ocean Optics spectrometers are accompanied by their software called SpectraSuite. This is a program which offers the user the complete functionality of the spectrometer. Unfortunately, for simple measurements it is often overly complicated. For that reason, a simpler program for measuring spectra has been written in MATLAB. Matlab supports the use of Ocean Optics' OmniDriver to communicate with the spectrometer.

The Graphical User Interface (GUI) of the program is shown in Figure D.1.
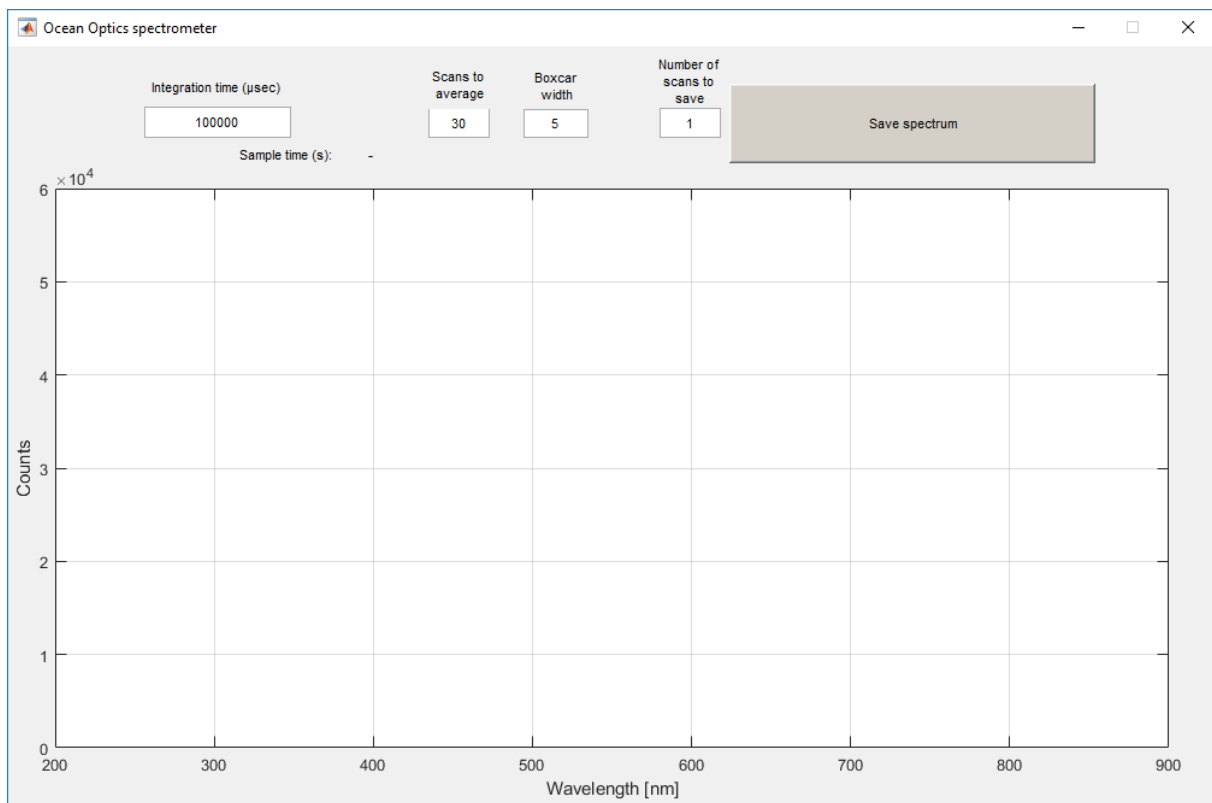

Figure D.1: Graphical User Interface of the MATLAB program for acquiring spectra.

The program defaults to the recommended settings as described by Ocean Optics [44]. The settings which can be changed are the integration time, scans to average, boxcar width and the number of scans to save. By default, the spectrometer records the spectra to a buffer. By acquiring a spectrum, the latest spectrum from the buffer is provided. However, the desired behavior is to start recording when the button is pressed. To achieve this, the acquirement of the spectrum is delayed by the sample time. This flushes the buffer such that the sample is recorded after the save button is pressed.

On pressing the save button, a dialog opens which asks where to save the spectrum. The saved file contains a line which displays the integration time used for acquiring the spectrum. Furthermore, it contains columns for the wavelength and counts measured at that wavelength.

The code is hosted on GitHub: https://github.com/stefanvanherwijnen/matlabspectrometer

E Spectrum post-processing

To prevent the requirement of SpectraSuite for post-processing, a MATLAB script has been written. This appendix provides a motivation for this approach and describes the basic functionality of the script.

SpectraSuite offers the option to calibrate a spectrometer with a known light source. By following the steps in the wizard, a calibration file is obtained. However, there is no documentation about the processing that is applied. Absolute irradiance data is acquired by loading the calibration file prior to the measurement. This leads to a major problem: the raw data cannot be validated (e.g. over-saturation or noise).

Fortunately, the calculations for calibration and measurements are relatively simple and documented by Ocean Optics. The basic formula to calculate the irradiance per pixel of the spectrometer is shown in Equation (E.1).

$$I_{e,\lambda} = C_{pixel} \left(\frac{S_{pixel} - D_{pixel}}{t \cdot A \cdot d\lambda} \right) \tag{E.1}$$

In which C_{pixel} stands for the calibration file [µJ count^{-1}], S_{pixel} for the sampled spectrum [counts], D_{pixel} for the dark spectrum [counts], t for the integration time of the acquired spectrum [s], A for the collection area [m^2] and $d\lambda$ for the wavelength spread [nm].

The lamp file provided with the light source contains the absolute irradiance at defined wavelenghts in µW nm^{-1} cm^{-2}. By measuring a normal and dark spectrum with a defined integration time and collection area, Equation (E.1) can be used to retrieve C_{pixel} in µJ count^{-1}.

As the lamp file only contains 21 data points in the wavelength range of 350 nm to 900 nm, the data has to be curve fitted. This comes along with another problem: a polynomial creates a poor fit. This is illustrated in Figure E.1.
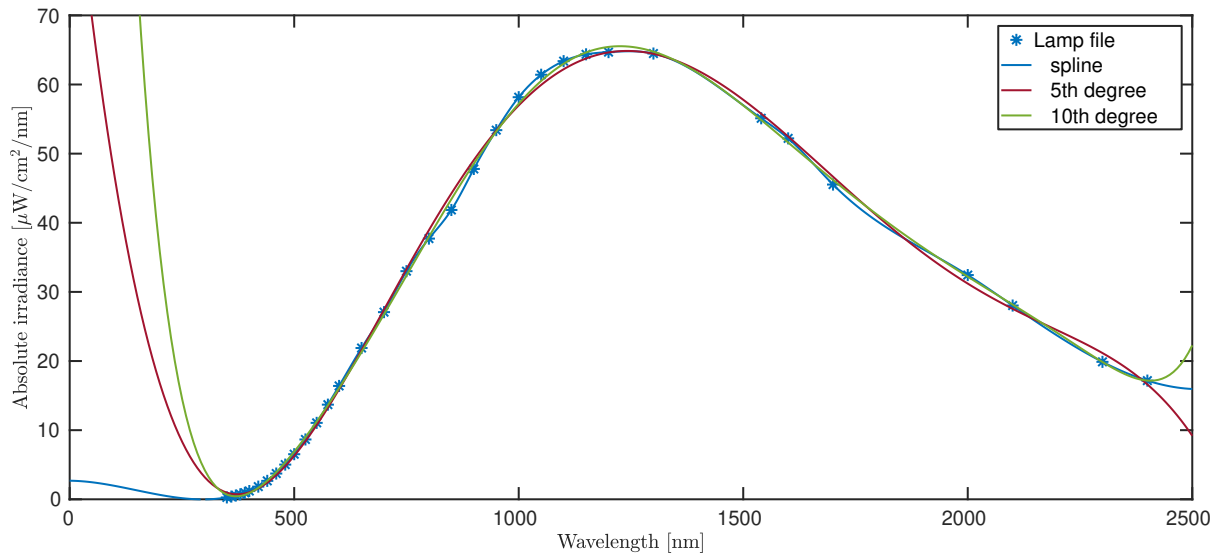

Figure E.1: Comparison of different curve fits of the data in the lamp file. It can be seen that the polynomial fits are inaccurate in some sections of the curve. They are also affected by Runge's phenomenon (oscillation at the edges of the interval).

The figure shows that polynomials do not fit the data very well. Especially in the range of 800 nm to 900 nm there is quite a large deviation of both polynomial fits from the data in the lamp file. Furthermore, the polynomials are affected by Runge's phenomenon (oscillation at the edges of the interval). Combined with a decreasing signal-to-noise ratio at the edges of the spectrometer detection range (200 nm to 900 nm) this will result in a significant measurement error. The effect is shown in Figure E.2.
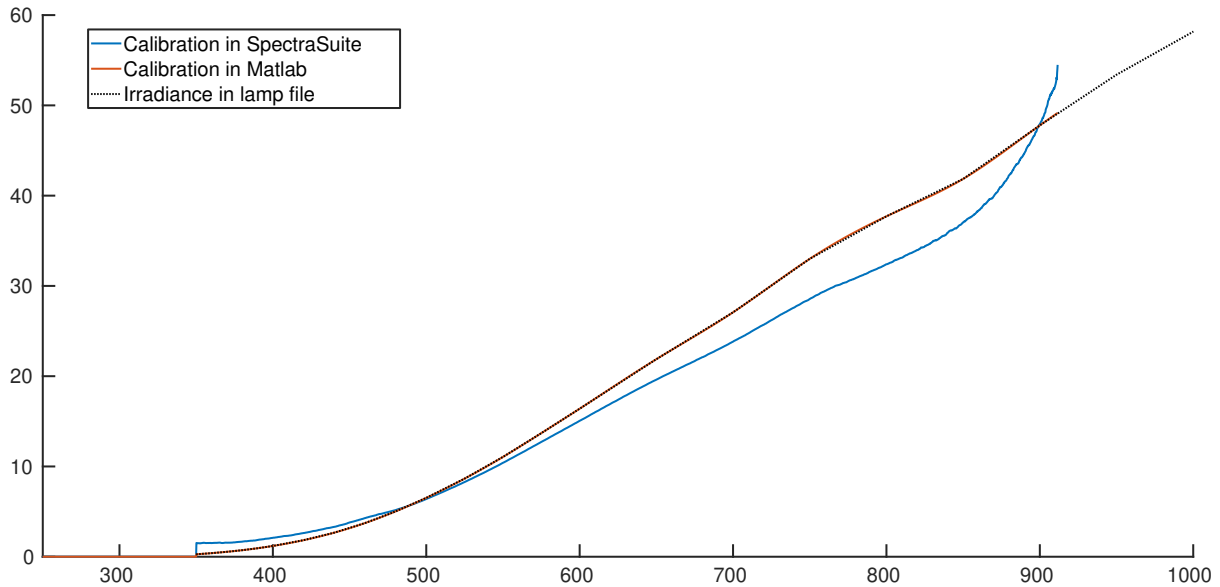

Figure E.2: Comparison of the application of the calibration file obtained from SpectraSuite and a manual calibration in MATLAB. The calibration files have been applied to a measurement of the light source, which means that the result should match the lamp file. It is clear that the calibration obtained from SpectraSuite deviates significantly from the irradiance as supplied in the light source's lamp file.

The figure has been created by measuring a raw spectrum of the light source and applying both calibration files to the data. The calibration in MATLAB has been created by applying spline interpolation to the lamp file data. The data of the lamp file is also plotted in the figure. It can be seen that the calibration obtained from SpectraSuite deviates significantly from the data in the lamp file. As there is no documentation of the actual processing in SpectraSuite, the exact cause can not be identified, but it is likely due to a poor curve fit as described before.

In order to obtain accurate irradiance values, raw spectra are manually processed in MATLAB. Two scripts have been written:

- createCalibrationFile() guides the user through the steps to create a file which contains the calibration data in $\mu J\,count^{-1}$.

- calculateIrradiance() provides the steps to calculate the absolute irradiance of a raw spectrum using the earlier created calibration file.

The scripts are also hosted on GitHub: https://github.com/stefanvanherwijnen/matlabspectrometer

F Curve fitting of Planck's law

In order to calculate the black body temperature of the acquired spectra, a curve fit of the data with Planck's law has been created in MATLAB. This appendix provides the used MATLAB scripts.

First, a MATLAB function for Planck's law has been written. The input arguments of the function are the black body temperature and a scaling factor. It returns the calculated spectral radiance. The function is shown below.

```matlab
function B = blackbody( param, wavelength )
%BLACKBODY Planck's law function
%    Function to generate a spectrum according to Planck's law by providing
%    a temperature and scaling factor.
h = 6.62607004081e-34;  % Planck constant
k = 1.3806485279e-23;   % Boltzmann constant
c = 299792458;          % Speed of light

T = param(1);
a = param(2);

lambda = wavelength * 1e-9; % Scale to nm
B = a .* ((2*h*c^2)./lambda.^5) .* 1./(exp((h*c)./(lambda*k*T)) - 1);

end
```

The function for Planck's law can then be used to obtain a curve fit with the optimization toolbox in MATLAB. The spectrum is first filtered by removing or smoothing the peaks. A curve fit is made based on this filtered spectrum. A theoretical spectrum is created by extending the acquired spectrum into the infrared range with the calculated black body temperature using Planck's law. The MATLAB function used for this is shown below.

```matlab
close all; clear all;

%% Settings the correct options for the curve fit
options = optimoptions('lsqcurvefit');
options.StepTolerance = 1e-12;
options.OptimalityTolerance = 1e-12;

%% Calculate absolute irradiance from the spectra and calibration file
spectrum = calculateAbsoluteIrradiance(0.39, 'calibration.mat', ...
    'lightSpectrum.txt', 'darkSpectrum.txt')

%% Smooth the spectrum and filter out the large peaks in UV
smoothed = medfilt1(spectrum.I(spectrum.wavelength > 450), 300);
wavelength = spectrum.wavelength(spectrum.wavelength > 450);

%% Create a best fit of the spectrum using Planck's law
bestfit = lsqcurvefit(@blackbody, [3300 1e-10], wavelength, ...
    smoothed, [], [], options)

%% Plot the spectrum, filtered spectrum and curve fit
figure; hold all;
maxI = max(spectrum.I);
plot(spectrum.wavelength, spectrum.I/maxI);
smplot = plot(wavelength, smoothed/maxI, '--');
plot(spectrum.wavelength, blackbody([bestfit(1), bestfit(2)], ...
    spectrum.wavelength)/maxI);

xlim([350 900])
legend('Magnesium flame spectrum', 'Filtered spectrum', ...
    ['Black body curve fit T = ' num2str(bestfit(1), 4) ' K'])
xlabel('Wavelength [nm]')
ylabel('Relative irradiance [-]');
figure;
```

```matlab
35  %% Extend the acquired spectrum with the calculated curve fit
36  theoreticalwavelength = [spectrum.wavelength(spectrum.wavelength ...
37      < 800)' [800:1:20000]];
38  theoreticalspectrum = [spectrum.I(spectrum.wavelength < 800)' ...
39      blackbody([bestfit(1), bestfit(2)], [800:1:20000])];
40  theoreticalspectrum = theoreticalspectrum / max(theoreticalspectrum);
41
42  %% Plot the extended spectrum
43  plot(theoreticalwavelength, theoreticalspectrum/max(theoreticalspectrum))
44
45  line([1100 1100], [0 0.5], 'Color', 'black', 'LineStyle', '-.')
46  total = trapz(theoreticalwavelength, theoreticalspectrum);
47  vis = trapz(theoreticalwavelength(theoreticalwavelength <= 1100), ...
48      theoreticalspectrum(theoreticalwavelength <= 1100)) / total
49  ir = trapz(theoreticalwavelength(theoreticalwavelength >= 1100), ...
50      theoreticalspectrum(theoreticalwavelength >= 1100)) / total
51
52  xlim([350 2000]);
53  text(900, 0.2, [num2str(vis*100, 3) '%']);
54  text(1200, 0.2, [num2str(ir*100, 3) '%']);
55  text(1120, 0.5, 'Silicon band gap');
56  ylabel('Relative irradiance [-]');
57  xlabel('Wavelength [nm]')
```

G Spectral mismatch

This appendix provides the used scripts to calculate the spectral mismatch between a given spectrum and a defined bandgap. As explained in Section 4.2.1, a semiconductor will only convert a finite amount of energy in a photon to electricity. This amount is defined by the bandgap.

To demonstrate this, the spectral mismatch has been calculated for the solar AM1.5 spectrum and a bandgap of $1.14\,\text{eV}$ (silicon).
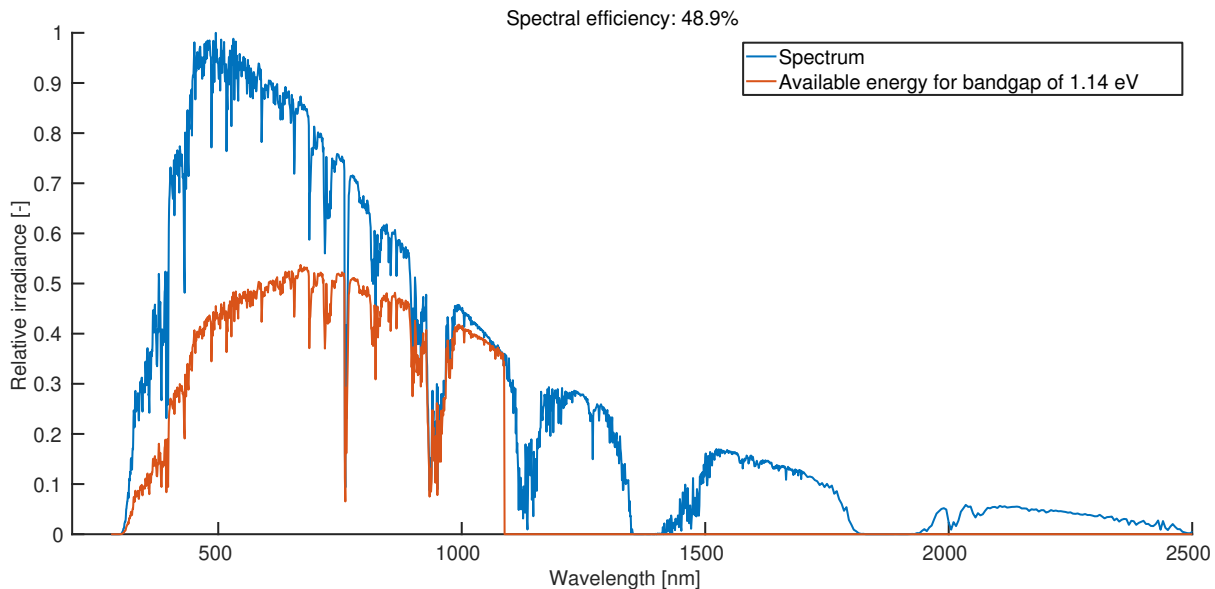

Figure G.1: Spectral mismatch between the solar AM1.5 spectrum and a silicon solar cell. It can be clearly seen that radiation with short wavelengths is only partially converted and for wavelengths above $1088\,\text{nm}$ it is not converted at all. This figure is also similar to Figure 3.5, although the used bandgap is slightly different.

The blue line shows the solar AM1.5 spectrum. The red line is calculated by multiplying the photon flux by the bandgap, as explained in Section 4.2.1. The maximum achievable efficiency based on the spectral mismatch is calculated by dividing the total absorbed energy by the total available energy. For the solar AM1.5 spectrum in combination with a silicon solar cell with a bandgap of $1.14\,\text{eV}$, this leads to an efficiency of 48.9%.

The efficiency of a multi-junction photovoltaic cell can also be calculated. By iterating over all combinations of bandgaps, the combination with the maximum efficiency can be calculated. For the solar AM1.5 this results in a bandgap of $1.53\,\text{eV}$ and $0.7\,\text{eV}$. The resulting spectral mismatch is shown in Figure G.2.
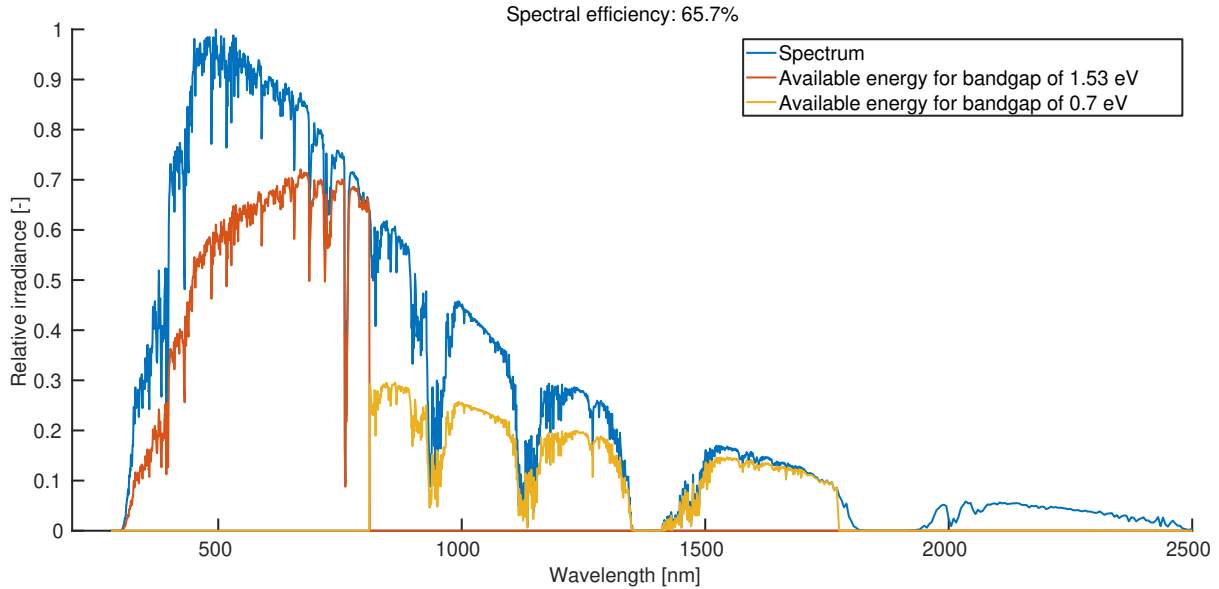
Figure G.2: Spectral mismatch between the solar AM1.5 spectrum and a multi-junction photovoltaic cell. The shown bandgaps achieve the theoretical maximum efficiency for a dual-junction photovoltaic cell.

Of course, this is a theoretical approach and the calculated bandgaps might not actually be achievable in a semiconducting material.

The function used for the calculations is shown below.

```matlab
function [ eff ] = multiJunctionMismatch ( spectrum, Eg, createPlot )
% MULTIJUNCTIONMISMATCH Calculate the spectral mismatch of a spectrum based on
% the provided band gap
%    Photons with an energy larger than the band gap energy of a
%    semiconductor are only partially converted to electricity. This
%    function calculates the spectral mismatch for a given spectrum and band
%    gap.

if (~exist('createPlot', 'var'))
    createPlot = 0;
end

EvtoJ = 1.602176565e-19;     % Conversion from eV to J [J]
Eg_J = Eg.*EvtoJ;            % Band gap [J]

h = 6.62607004081e-34;       % Planck constant
k = 1.3806485279e-23;        % Boltzmann constant
c = 299792458;               % Speed of light

bandgapwavelength = (h*c)./(Eg_J) * 1e9;     % [nm]

spectrum.I = spectrum.I/max(spectrum.I);     % scale to relative irradiance

%% Calculate spectral mismatch
% Photon flux [m^-2 s^-1 nm^-1]
photonflux = spectrum.I./(h*c./(spectrum.wavelength*1e-9));

% Total power available [W/m^2]
totalpower = trapz(spectrum.wavelength, spectrum.I);

% Available energy for band gap [W/m^2/nm]
availableenergy = [];
for (i = 1:length(bandgapwavelength))
```

72

```matlab
34        if (i == 1)
35            availableenergy(:,i) = photonflux .* Eg_J(i) .* (spectrum.wavelength ...
36            < bandgapwavelength(i));
37        else
38            availableenergy(:,end+1) = photonflux .* Eg_J(i) .* ( ...
39                bandgapwavelength(i-1) < spectrum.wavelength & ...
40                spectrum.wavelength < bandgapwavelength(i));
41        end
42        % Power available for defined band gap [W/m^2]
43        availablepower(i) = trapz(spectrum.wavelength, availableenergy(:,i));
44    end
45
46    % Efficiency based on spectral mismatch
47    eff = sum(availablepower/totalpower);
48
49    % Create plots
50    if (createPlot)
51        figure; hold all;
52        plot(spectrum.wavelength, spectrum.I);
53        for (i = 1:length(bandgapwavelength))
54            plot(spectrum.wavelength, availableenergy(:,i));
55        end
56
57        legendlabels{1} = 'Spectrum';
58        for (i = 1:length(Eg))
59            legendlabels{i+1} = ['Available energy for bandgap of ' num2str(Eg(i)) ' eV'];
60        end
61        legend(legendlabels)
62        xlabel('Wavelength [nm]');
63        ylabel('Relative irradiance [-]')
64        title(['Spectral efficiency: ' num2str(eff*100, 3) '%']);
65        xlim([200 2500])
66    end
```